MOX-Report No. 15/2020

An Image-based Computational Hemodynamics Study of the Systolic Anterior Motion of the Mitral Valve

Fumagalli, I.; Fedele, M.; Vergara, C.; Dede', L.; Ippolito, S.;

Nicolò, F.; Antona, C.; Scrofani, R.; Quarteroni, A.

MOX, Dipartimento di Matematica
Politecnico di Milano, Via Bonardi 9 - 20133 Milano (Italy)

mox-dmat@polimi.it http://mox.polimi.it

An Image-based Computational Hemodynamics Study of the Systolic Anterior Motion of the Mitral Valve *

Ivan Fumagalli[1], Marco Fedele[1], Christian Vergara[2], Luca Dede'[1], Sonia Ippolito[3], Francesca Nicolò[4], Carlo Antona[5], Roberto Scrofani[5], Alfio Quarteroni[1,6]

February 22, 2020

[1] MOX – Dipartimento di Matematica, Politecnico di Milano
[2] LABS – Dipartimento di Chimica, Materiali e Ingegneria Chimica "Giulio Natta", Politecnico di Milano
[3] Unità di Radiologia, Ospedale L. Sacco
[4] Dipartimento di Cardiochirurgia e dei Trapianti di Cuore, Azienda Ospedaliera San Camillo Forlanini
[5] Unità di Cardiochirurgia, Ospedale L. Sacco
[6] Mathematics Institute, École Polytechnique Fédérale de Lausanne (*Professor Emeritus*)

Keywords: Mitral valve, Hypertrophic Cardiomyopathy, Septal myectomy, Patient-specific simulations, Computational fluid dynamics, Image-based CFD

Abstract

Systolic Anterior Motion (SAM) of the mitral valve – often associated to Hypertrophic Obstructive Cardiomyopathy (HOCM) – is a cardiac pathology in which, during systole, a functional subaortic stenosis is induced by the mitral leaflets partially obstructing the outflow tract of the left ventricle. Its assessment by diagnostic tests is often difficult, possibly underestimating its severity and thus increasing the risk of sudden cardiac death. In the present work, the effects of SAM on the ventricular blood flow are investigated by means of Computational Fluid Dynamics (CFD) simulations. A novel image processing pipeline is set up to integrate cine-MRI data in the

*This project has received funding from the European Research Council (ERC) under the European Unions Horizon 2020 research and innovation programme (grant agreement No 740132, IHEART 2017-2022, P.I. A. Quarteroni). C. Vergara has been partially supported by the H2020-MSCA-ITN-2017, EU project 765374 "ROMSOC - Reduced Order Modelling, Simulation and Optimiza- tion of Coupled systems" and by the Italian research project MIUR PRIN17 2017AXL54F. "Modeling the heart across the scales: from cardiac cells to the whole organ"

numerical model. Patient-specific geometry and motion of the left ventricle are accounted for by an Arbitrary Lagrangian-Eulerian approach, and the reconstructed mitral valve is immersed in the computational domain by means of a resistive method. Clinically relevant flow and pressure indicators are assessed for different degrees of SAM severity, in order to separate the effects of SAM from those of HOCM. Our numerical results and study provide preliminary indications that help better evaluating pathological condition and the design of its surgical treatment.

1 Introduction

Systolic Anterior Motion (SAM) is a pathological condition of the heart where the anterior leaflet of the mitral valve is displaced towards the septum narrowing the Left Ventricle Outflow Tract (LVOT). This may lead to an unphysiologically high blood velocity through the LVOT and the aortic valve orifice, other than to an elevated intraventricular pressure gradient (Ibrahim et al. 2012; Jiang et al. 1987). SAM is often related to Hypertrophic Cardiomyopathy (HCM), which is a genetic disorder of the myocardium, characterized by marked myocardial hypertrophy (more than 15mm of wall thickness), with a prevalence of the $0.2 \div 0.6\%$ and an overall annual mortality rate of 1%, in the western world. In many cases, this condition can be asymptomatic for years, but it represents a risk of sudden cardiac death, particularly in young patients and athletes. When it affects the medio-basal portion of the septum, this condition takes the name of Hypertrophic Obstructive Cardiomyopathy (HOCM) and the LVOT obstruction that it entails is one of the main causes of SAM (Sherrid et al. 2016; Akiyama et al. 2017; Nicolò et al. 2019). The assessment of the SAM-induced pressure drop and shear stresses on the septum are of utmost importance for the clinical decision of possible surgical treatments such as septal myectomy, i.e. the resection of a portion of the septum (Ibrahim et al. 2012; Deng et al. 2018), and to decide whether such a procedure should be supplemented by valvuloplasty.

The present work is a computational study of HOCM-associated SAM and it has the purpose of proposing a methodology for the assessment of the pathological condition and providing preliminary clinical indications for its treatment. In particular, three main aspects are going to be covered:

- the blood flow in the ventricle and ascending aorta in the presence of SAM will be computationally analyzed, in order to assess the hemodynamic effects of this condition;
- preliminary clinical indications will be provided, that can help the surgeon in the preoperative design of septal myectomy;
- in order to fulfill the points above, a novel reconstruction pipeline will be proposed, to include diagnostic imaging data in the computational model.

Computational studies regarding the mitral valve dynamics and its interaction with blood flow in realistic scenarios have been proposed since the early 2000's. Fluid-structure interaction problems were considered for example by Kunzelman et al. 2007; Ma et al. 2013; Su et al. 2014; Lassila et al. 2017; Gao et al. 2017; Feng et al. 2019; Collia et al. 2019; Cai et al. 2019; Kaiser et al. 2019. On the other side, computational hemodynamics in prescribed kinematics settings has shown its suitability in studying blood flow patterns, as done by Otani et al. 2016; Tagliabue et al. 2017; Dedè et al. 2019; Masci et al. 2020. In this direction, the last decade has seen computational hemodynamics based on kinetic medical images become an effective tool to provide quantitative insights about cardiovascular diseases and useful indications to design clinical practices. Among the others, we mention: D'Elia et al. 2011, which used kinetic images of the aorta to reconstruct the motion of the vessel interface and to provide suitable boundary conditions at the vessel wall; the MRI-based study by Chnafa et al. 2016, where a discussion on turbulence in the left ventricle is carried on; the works by Seo et al. 2014; Bavo et al. 2017; This 2019; This et al. 2020, where CFD in the left ventricle is driven by the motion reconstructed from three-dimensional (3D) echocardiography data, see also Mittal et al. 2016 for a review on ventricular hemodynamics. However, CFD studies prescribing cardiac valve kinematics directly reconstructed by medical images have been scarcely used so far to describe ventricular blood flow, see Bavo et al. 2016, 2017. To the best of our knowledge, exploitation of cine-MRI in this context has not yet been performed, despite this technique is becoming increasingly important to study the cardiac function in clinics.

Moreover, patient-specific CFD studies of the blood flow in presence of SAM are rare. At the best of our knowledge, this topic has been addressed so far only by Deng et al. 2018, which have considered a fluid-structure interaction model to inspect the effectiveness of septal myectomy.

The aim of this work is to provide a CFD investigation and a numerical assessment of SAM based on kinetic imaging of both the Mitral Valve (MV) and the Left Ventricle (LV). In particular, the motion of the ventricle endocardium and of the mitral leaflets are reconstructed from cine-MRI data and employed to deform the computational domain and to prescribe boundary conditions to the blood flow model. Owing to these kinetic image-based data, we are able to obtain a computational framework that: i) avoids modeling the valve dynamics and myocardium mechanics, thus considerably reducing the computational effort; ii) embeds patient-specific geometric and functional data without any prior assumption on the model parameters; iii) avoids the modeling of the leaflets mechanics, which is a challenging task particularly in the pathological case; iv) hinges upon standard image data routinely acquired in current clinical practice.

Towards this goal, we propose a complete pipeline for image processing, consisting in the segmentation of left ventricle and mitral valve, the reconstruction of the corresponding motion through registration algorithms, the fulfillment of missing data by means of suitable interpolation procedures, and the use of a

template geometry of the human heart to integrate the anatomical data. Such a template allows completing the geometric data by including, e.g., the aorta and full 3D leaflets, that are usually not acquired during standard clinical imaging procedures.

In order to enable our computational hemodynamics study, we consider a mathematical model based on the Navier-Stokes equations defined in a moving domain, wherein we immerse the mitral valve leaflets according to a resistive method (Fernández et al. 2008; Astorino et al. 2012). In particular, we adopt the *resistive immersed implicit surface* (RIIS) model (Fedele et al. 2017) that enables dealing with a moving immersed surface in an Eulerian framework without explicitly building a surface-conforming mesh. In this framework, we perform a parametric study to assess the sensitivity of clinically meaningful indicators with respect to a parameter representative of the SAM-induced obstruction severity.

This numerical study has the potential to significantly impact on the clinical investigation and treatment of SAM. Indeed, understanding the HOCM-related changes in LV loading and contractility could be very difficult in the clinical setting, leading to an underestimation of the severity of SAM and of the risk of sudden cardiac death. Aiming at reducing such a risk, computational investigation, thanks to its fine spatial and temporal resolution, can identify many details that diagnostic tests such as transthoracic echocardiography or magnetic resonance cannot directly capture. Then, the resulting indications can also support the surgeon's decision on performing myectomy and/or mitral valvuloplasty.

The outline of the paper is as follows. In Section 2 we detail the pipeline of image processing that, starting from MRI images, allows reconstructing the geometry and motion of the ventricle (Section 2.1) and of the mitral valve (Section 2.2), and to include the aorta in the model (Section 2.3). In Section 3 we recall the resistive method for the mathematical description. Finally, in Section 4, we show several results obtained in a patient-specific setting, analyzing some useful hemodynamic quantities for different parametrizations of the SAM degree. Conclusions follow.

2 From image processing to geometric and functional data

In this section we illustrate the methods proposed to reconstruct the geometry and the movement of both the left ventricle endocardium (Section 2.1) and the mitral valve (Section 2.2), starting from medical images. Then, we delineate the strategy adopted to introduce the ascending aorta in the computational domain, by resorting to a template geometry (Section 2.3).

As input to our reconstruction procedure, we consider cardiac Magnetic Resonance Imaging (MRI). In the last years, cardiac MRI, including cine-MRI, has become the gold standard imaging technique to assess myocardial anatomy and global heart function (Karamitsos et al. 2009). This non-invasive technique has

been widely used both in the diagnosis of hypertrofic cardiomyopathy (Rickers et al. 2005; To et al. 2011; Maron 2012) and in the investigation of heart valve diseases (Myerson 2012; Myerson et al. 2016). Therefore MRI is the reference technique to diagnose SAM.

In Section 4.1, the procedure described in the present section will be applied to cine-MRI data of a patient provided by L. Sacco Hospital in Milan. These data come from standard clinical acquisitions, without the need of *ad hoc* imaging procedures for the purposes of the present work.

2.1 Reconstruction of the geometry and motion of the left ventricle endocardium

Cine-MRI has become a standard cardiac image data acquisition procedure, and it features a very accurate time resolution (at least 20 images per heartbeat). Concerning its space resolution, the so-called *short axis* view is typically the sole 3D representation available, whereas *long-axis* images are acquired only for few two-dimensional (2D) slices. More precisely, a long-axis image consists in a single 2D slice where the left ventricle is visible in all its extension from the apex to the base (see Fig. 1-b); on the contrary, short-axis views are made of a set of 2D images acquired orthogonally to the long-axis images at various equally spaced positions (see Fig. 1-a).

Short-axis cine-MRI are suitable for the left ventricle anatomy reconstruction for each available time of the heartbeat. However, due to the low resolution along the long axis, they are not sufficient to accurately reconstruct the movement of the left ventricle. Indeed, the shortening/stretching of the left ventricle along the long axis represents a relevant component of the ventricular contraction/relaxation. Moving from these considerations, we propose a pipeline to reconstruct both the geometry and the motion of the left ventricle endocardium, by combining information between short-axis and long-axis cine-MRI.

The proposed pipeline, which is sketched in Fig. 1, is comprised of the following steps:

1. for each acquisition instant, segmenting the 3D short-axis image (see Fig. 1-a) to produce a 3D surface of the left ventricle endocardium;

2. measuring the apex-to-base distance as a function of time in the long-axis image (see Fig. 1-b);

3. cutting at the base the 3D reconstructions of the endocardium obtained at step 1, coherently with the long-axis measurements obtained at step 2 (see Fig. 1-c);

4. modeling the cut surfaces as artificial high resolution level-set images (Fig. 1-d);

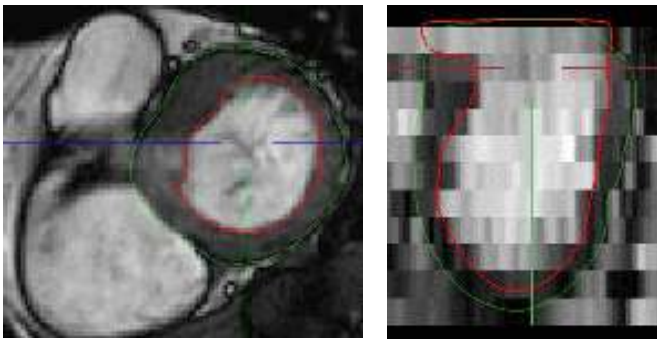

(a) Step 1.

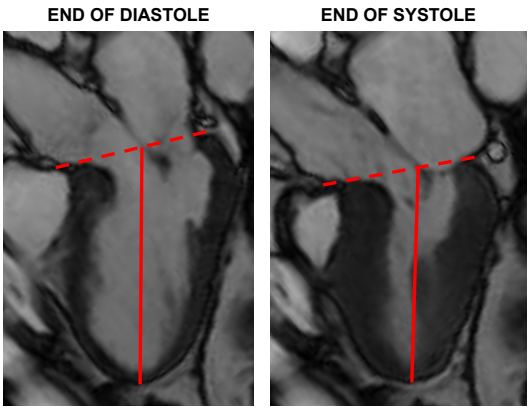

(b) Step 2.

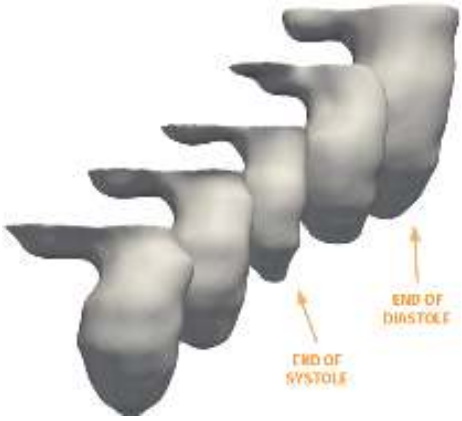

(c) Step 3.

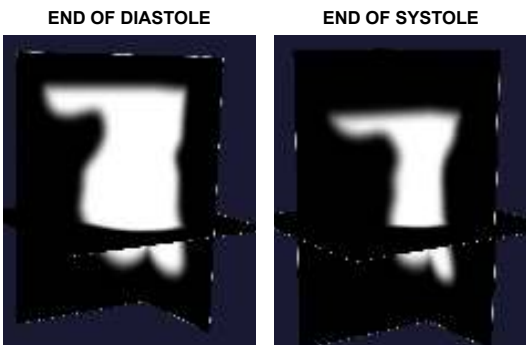

(d) Step 4.

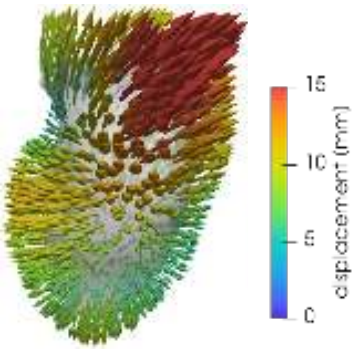

(e) Steps 5-6.

Figure 1: Pipeline to reconstruct the geometry and displacement of the left ventricle endocardium from cine-MRI: (a) short-axis 3D segmentation and corresponding endocardial surface reconstruction; (b) long-axis apex-to-base distance; (c) 3D surfaces obtained by merging the short- and long-axis information; (d) artificial level-set images created from the 3D surfaces; (e) final displacement field obtained by registering the artificial images with respect to the end-systolic instant.

5. introducing a reference configuration by fixing a time instant (e.g. the end of systole) and apply a registration algorithm among the artificial level-set images obtained at step 4 (see Fig. 1-e);

6. applying the transformation obtained by the registration to the 3D endocardium at the reference configuration (see Fig. 1-e).

Concerning the segmentation (step 1), different automatic or semi-automatic methods for the left ventricle reconstruction have been proposed in literature (Suri 2000; Lu et al. 2009), from the more classical methods based on thresholding and active contours (Lee et al. 2009) to the more recent techniques based on convolutional neural networks (Tran 2016; Tan et al. 2017). Our proposed pipeline is independent of the segmentation method adopted, the unique requirement being that the reconstructed endocardial surface accurately describes the pathological left ventricle of the patient. For this purpose, we adopt the semi-manual segmentation algorithm proposed by Fetzer et al. 2014 and implemented in the Medical Image Toolkit (MITK) (`www.mitk.org`) open source software (Wolf et al. 2005; Nolden et al. 2013). In particular, this algorithm is based on a manual identification of the endocardial 2D contours for a subset of the short-axis slices. Then, it automatically creates a 3D smooth surface exploiting a 3D radial basis function interpolation based on the intensity of the image and on the 2D contours. In Fig. 1-a we show the results of this method applied to our end-diastolic short-axis data.

In order to better reconstruct the motion of the ventricle, we aim at enriching our reconstruction with information about the ventricular shortening and stretching. These components of the motion can be measured from the long-axis images, in particular from the so-called *three chamber view*, where the left-ventricle is visible together with the left atrium and the aortic root. More in details, we measure the apex-to-base distance at each instants of this view (step 2, see Fig. 1-b) and we use these measures to select the portion of the segmented endocardium accordingly (step 3, see Fig. 1-c).

Then, we aim at registering all the reconstructed images at different instants. Roughly speaking, registration means recovering the geometric transformations or local displacements able to transform the configurations at each instant into the reference one. Registration algorithms are usually applied to images and their accuracy depends also on the resolution of the input image. However, we are not interested in the registration of the whole short-axis image with all the visible human organs (e.g. lungs, bones, ...), but only in the left ventricle endocardium. For this purpose, we model the endocardial surfaces of Fig. 1-c as artificial level-set images (step 4) as shown in Fig. 1-d. This choice allows creating images with the same resolution along each axis direction by extending the standard short-axis resolution to the long-axis direction.

Thus, the registration algorithm is applied to the artificial level-set images (step 5). As for the segmentation, our pipeline is independent of the particular

registration algorithm chosen. Moreover, since our input are the artificial level-set images which are of binary type, these can be easily registered using standard non-rigid registration algorithms (Crum et al. 2004; Hill et al. 2001; Oliveira and Tavares 2014). In particular, here we adopt the non-affine B-splines registration algorithm implemented in the *Elastix* open source library (`http://elastix.isi.uu.nl`, Klein et al. 2009).

For each time instant, the output of the registration is a 3D vector field defined in the whole 3D domain of the artificial image. This field can be evaluated at all the points of the reference endocardial surface (step 6). In this way, we are able to reconstruct, in the reference configuration of our left ventricle domain, a vector field describing the displacement of the endocardium in the whole heartbeat. In the following, by denoting with τ_{MRI} the time resolution of cine-MRI, we refer to such displacement field as $\mathbf{d}_{\text{MRI}}(t_k)$, being $t_k = k\,\tau_{\text{MRI}}$, $k = 0, \ldots, K = T/\tau_{\text{MRI}}$, the $K+1$ acquisition times of the cine-MRI and T the heartbeat duration. An example of this field, representing the displacement between the end-systolic configuration and the end-diastolic one, is shown in Fig. 1-e.

We remark that, despite the relatively fine temporal resolution of cine-MRI data if compared to other imaging techniques (e.g. CT-scans), the image sampling does not match the resolution needed for an accurate time discretization of the PDEs since the time step length of the latter is at least 10 times smaller than the cine-MRI resolution τ_{MRI}. For this reason, we need to interpolate the displacement field $\mathbf{d}_{\text{MRI}}(t_k)$ on a finer time grid, see Section 3.

2.2 Reconstruction of the geometry and motion of the mitral valve

As mentioned in the previous section, short-axis views of cine-MRI are well suited for the reconstruction of a chamber like the left ventricle. However, their resolution in the ventricular apex-to-base direction is much coarser (typically 8 mm) than along the other directions. On the other hand, typical long-axis views are time-dependent 2D images made of a single slice, orthogonal to the short axis of the ventricle, and they have a 1-mm resolution in the apex-to-base direction. Since the physiological thickness of valve leaflets is about 2 mm, we base our reconstruction of the mitral valve on long-axis views. In particular, we use the three-chambers view (see Fig. 2-a), that allows appreciating the distance between the anterior leaflet and the septum and thus the degree of stenosis induced by SAM. Since imaging data of a three-chambers view are made of a single 2D slice, the sole information concerning the mitral valve that can be extracted is a single line for each time t_k of the MRI acquisition. Thus, in order to have a complete 3D leaflet reconstruction, we complement this data by exploiting a template geometry (see also Section 2.3). For this purpose, we use the *Zygote solid 3D heart model* (Zygote Media Group, Inc. 2014), a complete heart geometry reconstructed from CT-scans representing an average

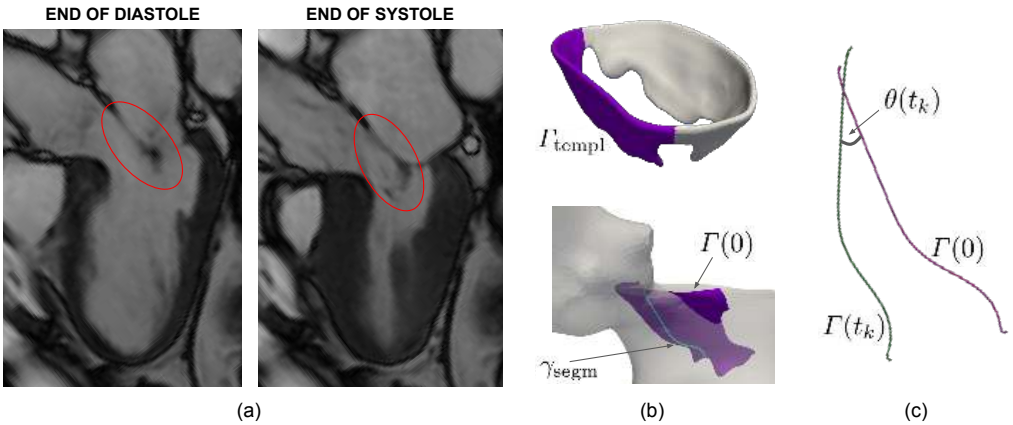

Figure 2: Mitral Valve (MV) reconstruction: (a) Anterior Mitral Leaflet (AML) in the three-chambers view; (b) Top: the Zygote AML template Γ_{templ} (in purple); Bottom: its morphing $\Gamma(0)$ onto the patient-specific leaflet, where the segmented centerline γ_{segm} is highlighted in green; (c) MV angle $\theta(t_k)$ w.r.t. end-diastolic configuration $\Gamma(0)$, defined between leaflet longitudinal centerlines.

healthy heart, including the mitral valve leaflets, see Fig. 2-b, top. Moreover, since SAM involves the displacement of the anterior mitral leaflet, we focus our reconstruction on such leaflet.

The pipeline to merge the information of the template geometry into the MRI data aims at obtaining the end-diastolic configuration of a patient-specific anterior mitral leaflet and goes through the following steps:

1. a surface Γ_{templ} describing the anterior mitral leaflet is extracted from the Zygote template mitral valve (see Fig. 2-b, top);

2. the leaflet longitudinal centerline γ_{segm} is segmented from the end-diastolic three-chambers view shown in Fig. 2-a, left;

3. the centerline obtained at step 2 is extruded in the normal direction to the three-chambers view plane, to obtain a surface Γ_{extr};

4. the template leaflet Γ_{templ} is projected onto the extruded surface Γ_{extr} to obtain the surface Γ representing the patient's MV anterior leaflet. The final result is shown in Fig. 2-b, bottom, together with the segmented leaflet centerline γ_{segm}.

The segmentation step 2 has been performed by means of MITK, while for the other steps, we developed ad hoc semi-automatic tools, based on the Visualization Toolkit (VTK, `vtk.org`) and the Vascular Modeling Toolkit (VMTK, `vmtk.org`, Antiga et al. 2008). At the end of this procedure, the reconstructed

surface $\Gamma = \Gamma(0)$ represents the configuration of the anterior mitral leaflet at the end of the diastolic phase, that is at $t = 0$.

In order to include the effects of the mitral valve in a time-dependent CFD simulation, the motion of the leaflet needs to be reconstructed. As our target is SAM, we focus on the systolic phase, that spans from the end-diastolic time $t = 0$ to the end-systolic time $t = T_{\mathrm{S}}$, thus accounting for K_S of the K frames available during the complete heartbeat.

We notice that during this phase, the leaflet progressively approaches the septum, without fluttering. The time evolution of the leaflet is then defined as rigid rotation of its end-diastolic configuration $\Gamma(0)$ around the normal direction of the three-chambers view. Accordingly, we introduce the angles $\theta(t_k)$, $k = 0, \ldots, K_S$, between the leaflet longitudinal centerline at the current configuration and the one at t_0, as shown in Fig. 2-c, and the associated displacement fields $\mathbf{d}_{\Gamma,\mathrm{MRI}}(\mathbf{x}, t_k)$ that map $\Gamma(0)$ to $\Gamma(t_k)$.

In view of our sensitivity study, starting from the actual value $\theta(T_S)$ characterizing the patient at hand, we also consider other two virtual values of $\theta(T_S)$, representing a milder and a stronger level of SAM severity, respectively. This will allow us to compare the results in terms of clinical outputs among different SAM scenarios.

2.3 Extension of the computational domain using a template geometry

In order to fully capture the hemodynamics effects of SAM, and to prevent boundary conditions from affecting our numerical results, we need to consider an extended computational domain that comprises the left ventricle and the ascending aorta. Unfortunately, standard cardiac cine-MRI are not sufficient for a 3D reconstruction of the ascending aorta, that is only partially visible in long-axis images (e.g. in the three-chambers view, see Fig. 2-a). For this reason, we propose here a strategy to properly merge, at the level of the LVOT, the patient-specific ventricular geometry and motion with a template ascending aorta obtained by the Zygote geometry (Zygote Media Group, Inc. 2014). Such a strategy consists of the following steps:

1. we start from two input surfaces: the reference end-diastolic patient-specific left ventricle endocardium - denoted hereafter as $\mathrm{LV}_{\mathrm{ps}}$ - and the upper part of the Zygote left heart - denoted as $\mathrm{LH}^{\mathrm{up}}_{\mathrm{zyg}}$. The former is the output of the segmentation cut at the mitral annulus and at the outflow tract. The latter is created by joining the internal surface of the Zygote left atrium with the ascending aorta;

2. we perform a rigid registration between the $\mathrm{LV}_{\mathrm{ps}}$ and $\mathrm{LH}^{\mathrm{up}}_{\mathrm{zyg}}$ ventricular rings using the Iterative Closest Point (ICP) algorithm (Besl and McKay 1992) (see Fig. 3-a);

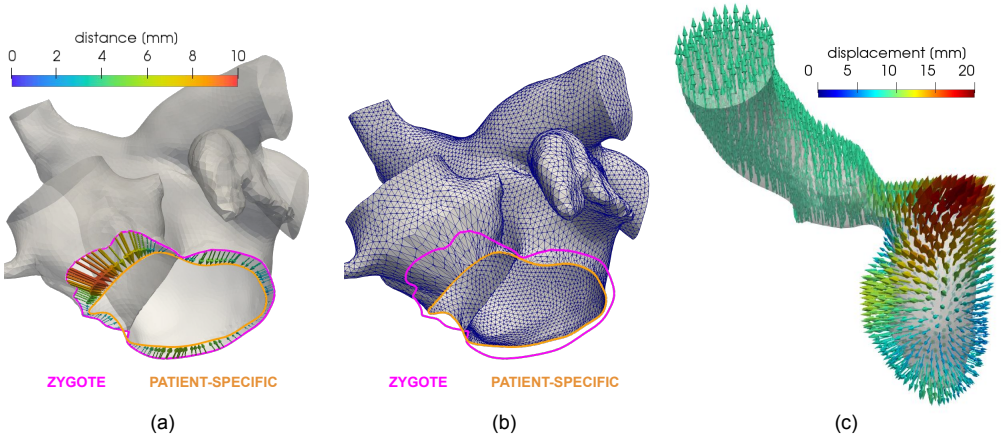

Figure 3: Part of the pipeline to merge the patient-specific left ventricle geometry and motion with the Zygote template ascending aorta: (a) ICP registration between the ventricular rings of the patient-specific ($\mathrm{LV}_{\mathrm{ps}}$) and of the template ($\mathrm{LH}^{\mathrm{up}}_{\mathrm{zyg}}$) surfaces. For visualization purposes, the ventricle is not depicted; (b) harmonic deformation of $\mathrm{LH}^{\mathrm{up}}_{\mathrm{zyg}}$ into $\mathrm{LV}_{\mathrm{ps}}$; (c) harmonic extension of the displacement field on the final computational domain without the left atrium.

3. we merge the two surfaces by deforming $\mathrm{LH}^{\mathrm{up}}_{\mathrm{zyg}}$ so that it conforms to $\mathrm{LV}_{\mathrm{ps}}$. The applied deformation is obtained as the solution of a Laplace-Beltrami problem (Antiga et al. 2003; Meyer et al. 2003) on a portion of $\mathrm{LH}^{\mathrm{up}}_{\mathrm{zyg}}$ near the ventricular ring. In particular, the vectorial distance between the two rings is used as a Dirichlet boundary condition (see Fig. 3-b);

4. since we are interested in the simulation of the systolic flow, we exclude the left atrium from the domain capping the mitral annulus;

5. eventually, we harmonically extend the displacement field $\mathbf{d}_{\mathrm{MRI}}(t_k)$ at the LVOT reconstructed from cine-MRI (see Section 2.1) in the ascending aorta and in the mitral annulus cap, using the same technique of step 3 (see Fig. 3-c).

All the described steps are performed by exploiting the VMTK library (Antiga et al. 2008) and the additional software tools for the cardiac meshing recently proposed in (Fedele 2019), to which we refer the interested reader for further details.

3 Mathematical and numerical modeling

We describe here the mathematical and numerical framework for the blood flow problem in a moving domain in presence of the mitral valve, which is reconstructed as described in Section 2. Let $\Omega(t)$ be the moving computational domain

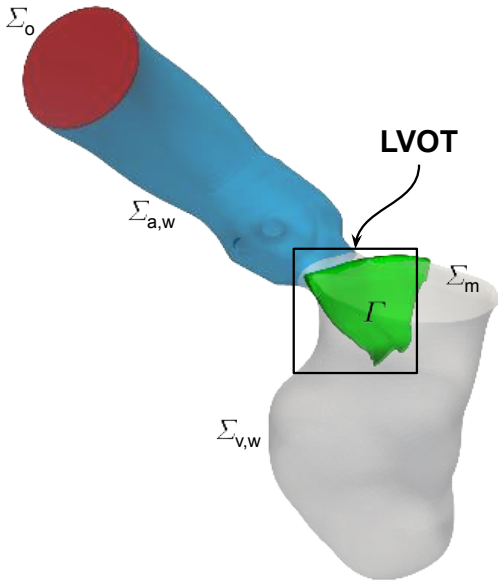

Figure 4: Computational domain $\Omega(t)$ with its ventricular (in grey) and aortic (in blue and red) boundaries, and the immersed mitral anterior leaflet surface $\Gamma(t)$ (in green). The LVOT is enclosed in a box.

made of the left ventricle and the ascending aorta; its boundary is partitioned into the following subsets, displayed in Fig. 4: the ventricular endocardium wall $\Sigma_{v,w}(t)$, the aortic wall $\Sigma_{a,w}(t)$, the mitral valve orifice $\Sigma_m(t)$, and the outflow section $\Sigma_o(t)$ located at the end of the aortic root. For the sake of convenience, we set $\Sigma(t) = \Sigma_{v,w}(t) \cup \Sigma_{a,w}(t)$.

The anterior leaflet of the mitral valve is described by a surface $\Gamma(t)$ immersed in $\Omega(t)$. Notice that Ω changes in time only due to the effect of the (prescribed) ventricular wall motion, which induces the movement of the aortic root (see Section 2). The contribution of the immersed mitral valve to blood dynamics is accounted for by means of a resistive method (Astorino et al. 2012; Fedele et al. 2017), as explained below. The motion of the domain and of the mitral leaflet are described by the displacement fields $\widehat{\mathbf{d}}_{\mathrm{MRI}}$ and $\widehat{\mathbf{d}}_{\Gamma,\mathrm{MRI}}$ referred to the end-diastolic configuration, reconstructed in Section 2. Since these fields are available only at the MRI acquisition times $t_k, k = 0, \ldots, K_{\mathrm{S}}$, time interpolation is employed to define such displacements for all $t \in [0, T_{\mathrm{S}})$ of the systolic phase. Indeed, being SAM a pathology that pertains to systole, we focus our study only on this phase of the heartbeat.

We consider blood as an incompressible Newtonian fluid with uniform density ρ and viscosity μ. The ventricle contraction can be taken into account by solving the fluid problem at each time $t > 0$ by means of an *Arbitrary Lagrangian-Eulerian* (ALE) approach (cf., e.g., Donea et al. 1982; Nobile and

Formaggia 1999). The presence of the mitral valve is accounted for by the Resistive Immersed Implicit Surface (RIIS) method, introduced by Fedele et al. 2017; see also Fernández et al. 2008; Astorino et al. 2012 for other resistive methods. This method consists in the introduction of an additional term in the momentum equation, which penalizes the kinematic condition, i.e. the adherence of the blood to the moving leaflet. Thus, the continuous problem reads:

$$\begin{cases} \rho\partial_t^{\mathrm{ALE}}\mathbf{u} + \rho\left(\mathbf{u}-\mathbf{u}_{\mathrm{ALE}}\right)\cdot\nabla\mathbf{u} - \nabla\cdot\boldsymbol{\sigma}(\mathbf{u},p) & \\ \qquad +\frac{R}{\varepsilon}(\mathbf{u}-\mathbf{u}_\Gamma)\delta_{\Gamma,\varepsilon} = \mathbf{0} & \text{in } \Omega(t), \\ \nabla\cdot\mathbf{u} = 0 & \text{in } \Omega(t), \\ \mathbf{u} = \mathbf{u}_{\mathrm{MRI}} & \text{on } \Sigma(t), \\ \mathbf{u} = \mathbf{u}_{\mathrm{m}} & \text{on } \Sigma_{\mathrm{m}}(t), \\ \boldsymbol{\sigma}\mathbf{n} = p_{\mathrm{o}}\mathbf{n} & \text{on } \Sigma_{\mathrm{o}}(t), \\ \mathbf{u}(0) = \mathbf{u}^0 & \text{in } \Omega(0), \end{cases} \tag{1}$$

where $\mathbf{u}, p$ are the blood velocity and pressure, $\boldsymbol{\sigma} = \mu(\nabla\mathbf{u} + \nabla\mathbf{u}^T) - pI$ the corresponding Cauchy stress tensor, $\partial_t^{\mathrm{ALE}}$ is the time derivative in the ALE framework, and $\mathbf{u}_{\mathrm{ALE}}$ the fluid domain velocity. The latter is defined in $\Omega(t)$ as $\mathbf{u}_{\mathrm{ALE}} = \left(\frac{d}{dt}\widehat{\mathbf{d}}\right)\circ\widehat{\mathbf{d}}^{-1}$, namely as the time derivative of the fluid domain displacement $\widehat{\mathbf{d}}$, which is the solution to the following harmonic extension problem, for each $t \in (0, T_{\mathrm{S}}]$:

$$\begin{cases} -\Delta\widehat{\mathbf{d}}(\mathbf{x},t) = \mathbf{0} & \text{in } \Omega(0), \\ \widehat{\mathbf{d}}(\mathbf{x},t) = \widehat{\mathbf{d}}_{\mathrm{MRI}}(\mathbf{x},t) & \text{on } \Sigma(0)\cup\Sigma_m(0), \\ \partial_{\mathbf{n}}\widehat{\mathbf{d}}(\mathbf{x},t) = \mathbf{0} & \text{on } \Sigma_{\mathrm{o}}(0). \end{cases}$$

The velocity fields $\mathbf{u}_{\mathrm{MRI}}, \mathbf{u}_{\mathrm{m}}$ are defined in a similar way, resorting directly to the reconstructed field $\widehat{\mathbf{d}}_{\mathrm{MRI}}$. The resistive term penalizing the leaflet velocity, with a resistance coefficient R, has support in a narrow layer around Γ represented by a smoothed Dirac delta type function

$$\delta_{\Gamma,\varepsilon}(\varphi) = \begin{cases} \dfrac{1+\cos(2\pi\varphi/\varepsilon)}{2\varepsilon} & \text{if } |\varphi| \le \varepsilon, \\ 0 & \text{if } |\varphi| > \varepsilon, \end{cases}$$

where φ is a signed distance function that implicitly describes the immersed surface as $\Gamma = \{\mathbf{x}\colon \varphi(\mathbf{x}) = 0\}$, and $\varepsilon > 0$ is a suitable parameter representing half of the thickness of the leaflet. The prescribed leaflet velocity $\mathbf{u}_\Gamma$ may be provided in different ways, with computational costs progressively diminishing along the following order: (i) as the solution to an additional structural problem for the leaflet; (ii) by a reconstruction procedure based on clinical data; (iii) adopting a quasi-static approach, that is setting $\mathbf{u}_\Gamma \equiv \mathbf{0}$. In the present work, we deem the third option as a suitable approximation: indeed, an estimate of the

SAM-induced leaflet tip velocity based on clinical observations is on the order of 0.03 m/s, which is much lower than 1 m/s, the characteristic blood velocity in the LVOT.

Regarding boundary conditions for (1), we point out that the scalar $p_{\mathrm{o}}(t)$ is a prescribed stress at the outflow section, standing for the aortic pressure, whereas the mitral valve orifice Σ_{m} is kept close and follows the wall motion, since only the systolic phase is considered. Notice also that the aortic orifice is always open, thus justifying our choice to neglect the aortic valve leaflets. Indeed, our attention is on the intraventricular pressure drop and on the stenosis induced by the SAM of the mitral valve.

Remark 3.1 *The RIIS term in* (1) *penalizes the kinematic condition* $\mathbf{u} = \mathbf{u}_\Gamma$ *on* Γ. *As a matter of fact, the RIIS method is one of the possible strategies to account for an immersed surface; some of its features are shared with other methods available in the literature. It has many points in common with the immersed boundary method (Peskin 1972; Boffi and Gastaldi 2003; Iaccarino and Verzicco 2003; Mittal and Iaccarino 2005; Taira and Colonius 2007; Borazjani 2013), but its reduced computational cost is comparable with that of the Resistive Immersed Surface (RIS) method (Fernández et al. 2008; Astorino et al. 2012). The main advantage w.r.t. the latter is that the computational mesh and the surface* Γ *do not need to be conforming.*

Remark 3.2 *In the context of cardiac hemodynamics with valves, several approaches are proposed in the literature to account for moving surfaces inside a fluid domain. The variety of the methods can be roughly grouped into two categories: those which entail updating the fluid computational mesh through time, near the moving surface, and those in which the fluid mesh is independent of the immersed surface. The first category comprises the ALE approach (Cheng et al. 2004; Morsi et al. 2007; Espino et al. 2014; Basting et al. 2017), cutFEM/XFEM methods (Massing et al. 2015; Alauzet et al. 2016; Zonca et al. 2018; Boilevin-Kayl et al. 2019b) amd chimera overset grid methods (Ge et al. 2005; Le and Sotiropoulos 2013). The second category is mainly made of immersed-boundary / fictitious-domain methods (De Hart et al. 2003; Yu 2005; van Loon et al. 2006; Dos Santos et al. 2008; Astorino et al. 2009; Griffith et al. 2009; Borazjani et al. 2010; Ge and Sotiropoulos 2010; Griffith 2012; Hsu et al. 2014; Kamensky et al. 2015; Boilevin-Kayl et al. 2019a; Wu et al. 2018; Kaiser et al. 2019). In general, this second approach - shared also by the RIIS method - entails a lower computational cost, and it can be more easily applied to challenging patient-specific geometries. For a more thorough review about the modeling of heart valves, we refer the reader to Yoganathan et al. 2005; Sotiropoulos and Borazjani 2009; Votta et al. 2013; Marom 2015; Mittal et al. 2016; Quarteroni et al. 2019.*

In order to numerically solve problem (1), a stabilized piecewise linear finite element approximation is adopted, with a semi-implicit Euler scheme over a uniform partition $t^n = n\Delta t$, $n = 0, 1, \ldots$, of the time interval. At the end-diastolic

time $t = 0$, the fluid domain $\Omega^0 = \Omega(0)$ is triangulated into a the computational mesh $\mathcal{T}_h^0$, h being the maximum diameter of the mesh elements, and the piecewise linear finite element spaces V_h^0, Q_h^0 are introduced for the velocity and pressure variables $\mathbf{u}_h$ and p_h. Then, at each time step, a displacement field $\mathbf{d}_h^n$, $n = 1, 2, \ldots$ is introduced in terms of the reconstructed field $\widehat{\mathbf{d}}_{\text{MRI}}$ and employed to update the computational mesh and the space, before solving the fluid problem. We remind that the geometrical data $\widehat{\mathbf{d}}_{\text{MRI}}$ and $\widehat{\mathbf{d}}_{\Gamma,\text{MRI}}$, obtained as described in Sections 2.1 and 2.2, respectively, are defined on a different partition of the time interval w.r.t. the simulation time instants t^n just introduced. Therefore, piecewise linear interpolation in time is employed, to project such quantities onto the simulation time discretization. In these settings, the outline of the solution procedure is the following:
Let Ω^n be the computational domain approximating $\Omega(t^n)$. The quantities at time t^n are known. Then, for each $n = 0, 1, \ldots,$

1. Compute the displacement $\mathbf{d}_{\text{MRI}}^{n+1} : \partial\Omega^{n+1} \to \mathbb{R}^3$, from the datum $\widehat{\mathbf{d}}_{\text{MRI}}$, by time interpolation between the (coarser) MRI temporal sub-intervals $\{t_k = k\tau_{\text{MRI}},\ k = 0, \ldots, K_{\text{S}}\}$ and the (finer) simulation time discretization $\{t^n = n\Delta t,\ n = 0, \ldots, N_{\text{S}}\}$;

2. Solve the ALE harmonic extension problem:

$$\text{Find } \widehat{\mathbf{d}}_h^{n+1} \in V_h^0 \quad \text{s.t.}$$
$$\left(\nabla\widehat{\mathbf{d}}_h^{n+1}, \nabla\widehat{\mathbf{v}}_h\right) = 0 \quad \forall \mathbf{v}_h \in V_h^0, \qquad \text{and} \quad \widehat{\mathbf{d}}_h^{n+1}|_{\partial\Omega^n} = \widehat{\mathbf{d}}_{\text{MRI}}^{n+1},$$

   and then compute the numerical ALE velocity

$$\widehat{\mathbf{u}}_{\text{ALE},h}^{n+1} = \frac{\widehat{\mathbf{d}}_h^{n+1} - \widehat{\mathbf{d}}_h^n}{\Delta t};$$

3. Move the domain and the mesh according to the ALE map $\mathcal{A}^{n+1} : \Omega^0 \to \mathbb{R}^3$, $\mathcal{A}^{n+1}(\mathbf{x}) = \mathbf{x} + \widehat{\mathbf{d}}_h^{n+1}$:

$$\Omega^{n+1} = \mathcal{A}^{n+1}(\Omega^0), \qquad \mathcal{T}_h^{n+1} = \mathcal{A}^{n+1}(\mathcal{T}_h^0),$$

   and update the spaces V_h^n, Q_h^n to V_h^{n+1}, Q_h^{n+1}.

4. Update the position Γ^{n+1} of the immersed mitral leaflet, according to a time interpolation of the displacement $\widehat{\mathbf{d}}_{\Gamma,\text{MRI}}$;

5. Solve a time step of the SUPG-stabilized, linear discrete fluid problem, obtained by a semi-implicit first order approach:

$$
\begin{aligned}
&\text{Find } (\mathbf{u}_h^{n+1}, p_h^{n+1}) \in V_h^{n+1} \times Q_h^{n+1} \text{ such that} \\
&\left(\frac{\rho}{\Delta t}\mathbf{u}_h^{n+1} + \rho(\mathbf{u}_h^n - \mathbf{u}_{\mathrm{ALE},h}^{n+1}) \cdot \nabla \mathbf{u}_h^{n+1}, \mathbf{v}_h\right)_{\Omega^{n+1}} + \left(\boldsymbol{\sigma}_h^{n+1}, \nabla \mathbf{v}_h\right)_{\Omega^{n+1}} \\
&\quad + \left(\nabla \cdot \mathbf{u}_h^{n+1}, q_h\right)_{\Omega^{n+1}} + \frac{R}{\varepsilon}\left(\mathbf{u}_h^{n+1}, \delta_{\Gamma^{n+1},\varepsilon}\, \mathbf{v}_h\right)_{\Omega^{n+1}} \\
&\quad + (\tau_{\mathrm{M}}(\mathbf{u}_h^n - \mathbf{u}_{\mathrm{ALE},h}^{n+1})\mathbf{r}_{\mathrm{M}}^{n+1}(\mathbf{u}_h^{n+1}, p_h^{n+1}), \rho(\mathbf{u}_h^n - \mathbf{u}_{\mathrm{ALE},h}^{n+1}) \cdot \nabla \mathbf{v}_h + \nabla q_h)_{\Omega^{n+1}} \\
&\quad + (\tau_{\mathrm{C}}(\mathbf{u}_h^n - \mathbf{u}_{\mathrm{ALE},h}^{n+1}) r_{\mathrm{C}}(\mathbf{u}_h^{n+1}), \nabla \cdot \mathbf{v}_h)_{\Omega^{n+1}} \\
&= \left(\frac{\rho}{\Delta t}\mathbf{u}_h^n, \mathbf{v}_h\right)_{\Omega^n} + \int_{\Sigma_{\mathrm{o}}^{n+1}} p_{\mathrm{o}}(t^{n+1}) \mathbf{n} \cdot \mathbf{v}_h \, d\Sigma \\
&\forall (\mathbf{v}_h, q_h) \in V_h^{n+1} \times Q_h^{n+1}, \\
&\text{with } \mathbf{u}_h^{n+1} = \mathbf{u}_{\mathrm{ALE},h}^{n+1} \text{ on } \Sigma^{n+1} \cup \Sigma_{\mathrm{m}}^{n+1}, \quad \text{being} \\
&\tau_{\mathrm{M}}(\mathbf{u}) = \left(\frac{\rho^2}{\Delta t^2} + \frac{\rho^2}{h_K^2}|\mathbf{u}|^2 + 30\frac{\mu^2}{h_K^4} + \frac{R^2}{\varepsilon^2}\delta_{\Gamma^{n+1},\varepsilon}^2\right)^{-1/2}, \\
&\tau_{\mathrm{C}}(\mathbf{u}) = \frac{h_K^2}{\tau_{\mathrm{M}}(\mathbf{u})}, \\
&\mathbf{r}_{\mathrm{M}}^{n+1}(\mathbf{u}, p) = \rho\left(\frac{\mathbf{u} - \mathbf{u}_h^n}{\Delta t} + (\mathbf{u}_h^n - \mathbf{u}_{\mathrm{ALE},h}^{n+1}) \cdot \nabla \mathbf{u}\right) \\
&\qquad\qquad + \nabla p - \mu \Delta \mathbf{u} + \frac{R}{\varepsilon}\delta_{\Gamma^{n+1},\varepsilon}\mathbf{u}, \\
&r_{\mathrm{C}}(\mathbf{u}) = \nabla \cdot \mathbf{u},
\end{aligned}
$$

where $(\cdot,\cdot)_X$ denotes the scalar product in X. The scheme is stabilized by the SUPG/PSPG method (Tezduyar and Sathe 2003). The stabilization parameters τ_{M} and τ_{C} are chosen according to the variational multiscale approach (Bazilevs et al. 2007; Forti and Dedè 2015). In particular, they depend on the local mesh size h_K and on the local velocity magnitude. This numerical method was adapted for the RIIS model in a rigid domain by Fedele et al. 2017 and it is extended here to the ALE case.

4 Numerical results

The reconstruction procedures and the numerical method described in the previous sections are applied to the cine-MRI of a female patient provided by L. Sacco Hospital in Milan. The study has been approved by the Ethics Committee according to institutional ethics guidelines. The patient gave her signed consent for the publication of data. This patient suffered from SAM of the mitral valve and Hypertrophic Obstructive Cardiomyopathy (HOCM), particularly significant in the interventricular septum. No MV regurgitation has been reported. The dimensions of the LV blood chamber (end-diastolic volume of

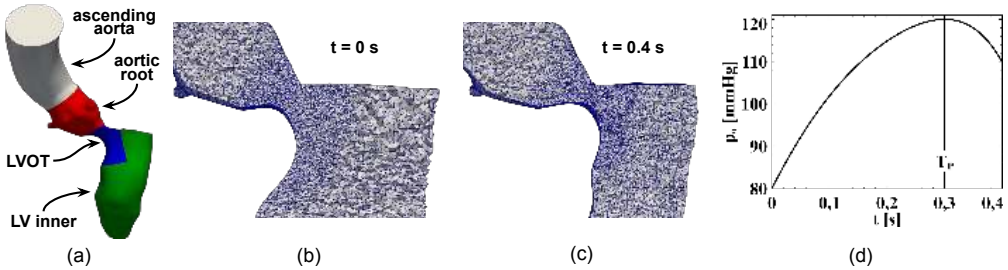

Figure 5: Computational domain and boundary conditions. (a) Significant regions of the computational domain: main portion of the LV (LV inner, in green), LVOT (blue), aortic root (red) and ascending aorta (grey); (b)-(c) clip of the CFD mesh in the LVOT at the initial time ($t = 0\,s$) and at the end of systole ($t = 0.4\,s$); (d) time evolution of the imposed aortic pressure p_{o}.

100.8 ml) and its global systolic function (ejection fraction of 63%) lay within the limits of non-pathological conditions. Moreover, an increased mass has been measured (indexed end-diastolic wall mass of 59.9 g) and the thickness and the systolic thickening of the myocardium are typical of hypertrophic cardiomyopathy. This condition, combined with the pathological motion of the MV anterior leaflet during systole, determines an intraventricular stenosis, whose effects on hemodynamic quantities are investigated by using our numerical software.

The results presented in the following sections are threefold:

1. in Section 4.1, we report the outcome of the reconstruction pipeline described in Section 2, that provides the endocardium displacement $\mathbf{d}_{\mathrm{MRI}}$ and the configurations of the mitral valve Γ for different levels of SAM severity;

2. in Section 4.2, the effect of SAM severity on hemodynamic quantities is assessed by means of CFD results;

3. in Section 4.3, we focus on some specific quantities in order to provide useful indications for the design of septal myectomy, a possible surgical treatment for the patient's condition.

In Fig. 5-a we highlight some significant regions of the computational domain, exploited in Sections 4.2 and 4.3 to compute relevant fluid dynamics quantitities. The computational results of these sections are obtained by means of the finite element library LifeV (Bertagna et al. 2017, `www.lifev.org`) on the tetrahedral mesh shown in Fig. 5-b,c for the initial time $t = 0$ and the end of systole $t = T_{\mathrm{S}}$. An average mesh size of $h = 1.2\,mm$ is chosen for most of the fluid domain, while a refinement to $h = 0.6\,mm$ is considered in the LVOT. Each simulation ran for about 5.3 days on 2 processors with 24 cores Intel(R) Xeon(R) Platinum 8160 CPU (2.10GHz) each, in a HPC node with 1.5TB RAM.

ρ $\left[\frac{\text{kg}}{\text{m}^3}\right]$	μ $\left[\frac{\text{kg}}{\text{m s}}\right]$	R $\left[\frac{\text{kg}}{\text{m s}}\right]$	ε [m]	T_{S} [s]	Δt [s]
10^{-3}	$3.5 \cdot 10^{-3}$	10000	$7 \cdot 10^{-4}$	0.4	$2.5 \cdot 10^{-4}$

Table 1: Parameters of the simulations.

The physical parameters of the model and the time discretization are reported in Table 1. Concerning the resistive method with resistance R, the characteristic length ε is chosen to ensure that the corresponding smeared Dirac delta $\delta_{\Gamma,\varepsilon}$ spans over two mesh elements (Fedele et al. 2017). Regarding boundary conditions, since we are interested in the systolic phase, the mitral orifice is closed by a no-flow condition ($\mathbf{u}_{\text{m}} = \mathbf{u}_{\text{ALE}}$ on Σ_{m} in (1)), whereas a time-dependent pressure p_{o} is applied as Neumann condition to the outflow section of the ascending aorta (see (1)), reported in Fig. 5-d, and representing a physiological behavior taken from Wiggers diagrams (Wiggers 1923; Mitchell and Wang 2014). We point out that p_{o} attains its maximum at $t = 0.3s$: in the following, we will refer to this time instant as the *systolic peak* $T_{\text{P}} = 0.3s$.

4.1 Application of the reconstruction pipeline

Employing the segmentation and registration pipelines described in Sections 2.1 and 2.2, the kinematics of the left ventricle and of the mitral valve have been reconstructed from cine-MRI.

The reconstructed displacement field $\mathbf{d}_{\text{MRI}}$ of the endocardium surface is shown in Fig. 6. Observe that this motion well captures the macroscopic contraction and shortening of the ventricular chamber, as well as the displacement variations characterizing the hypertrophy of the cardiac muscle.

In order to assess the reliability of the LV reconstruction in terms of the available clinical measurements, the time evolution of the LV cavity volume is reported in Fig. 7. The shape of the volume curve well represents the behavior of the LV as known from Wiggers diagram (Wiggers 1923; Mitchell and Wang 2014). Moreover, comparing the values of the reconstructed End Diastolic Volume (EDV) and Ejection Fraction (EF) with those measured during the clinical acquisition, we notice a substantially good agreement, see Table 2. In this respect, it is worth to point out that the measure of the volume provided in clinical tests is obtained from the length of the two main LV axes and having regarded the LV as an ellipsoid. This represents a coarse approximation of the actual LV geometry, and the discrepancies w.r.t. our reconstructed measures can be ascribed to it.

In order to study the effect of SAM on blood flow quantities in the LVOT (see Figs. 4 and 5-a), we consider three SAM severity scenarios, identified by different values of the end-systolic angle $\theta(T_S)$, see Fig. 2-c. In particular, we use the angle $\theta(T_S) = 25°$ that characterizes the actual patient condition (PS),

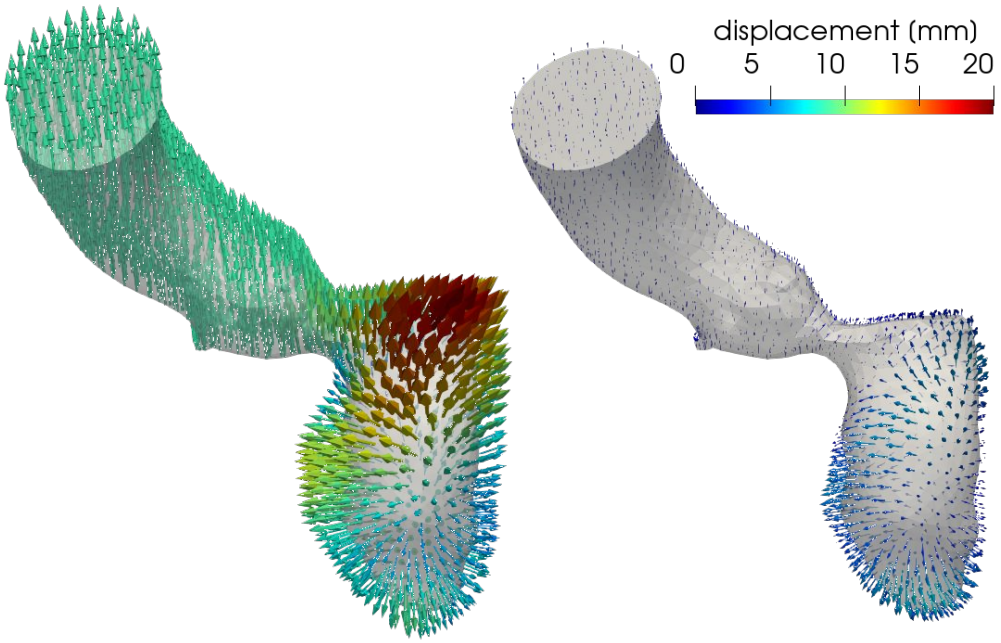

Figure 6: Displacement field $\mathbf{d}_{\mathrm{MRI}}$ of the LV endocardium with respect to its end-systolic configuration: on the left, initial systolic configuration ($t_0 = 0\,s$); on the right, mid-diastolic configuration ($t_{12} = 0.6\,s$).

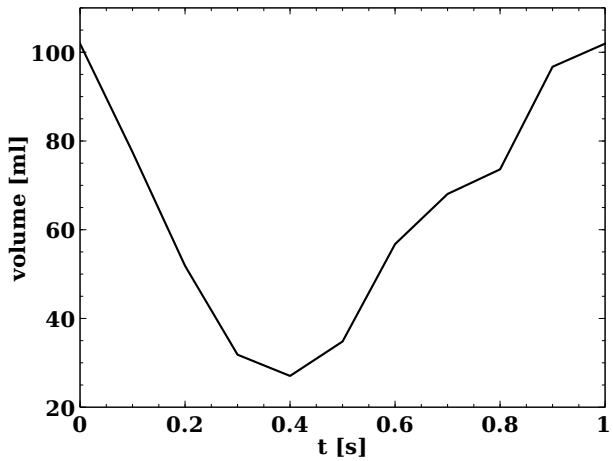

Figure 7: Time evolution of the reconstructed LV cavity volume.

	clinical	reconstructed
EDV [mL]:	100.8	102.0
EF [-] :	0.63	0.72

Table 2: Volumetric values from the clinical report and from the current reconstruction: end-diastolic volume (EDV) and ejection fraction (EF).

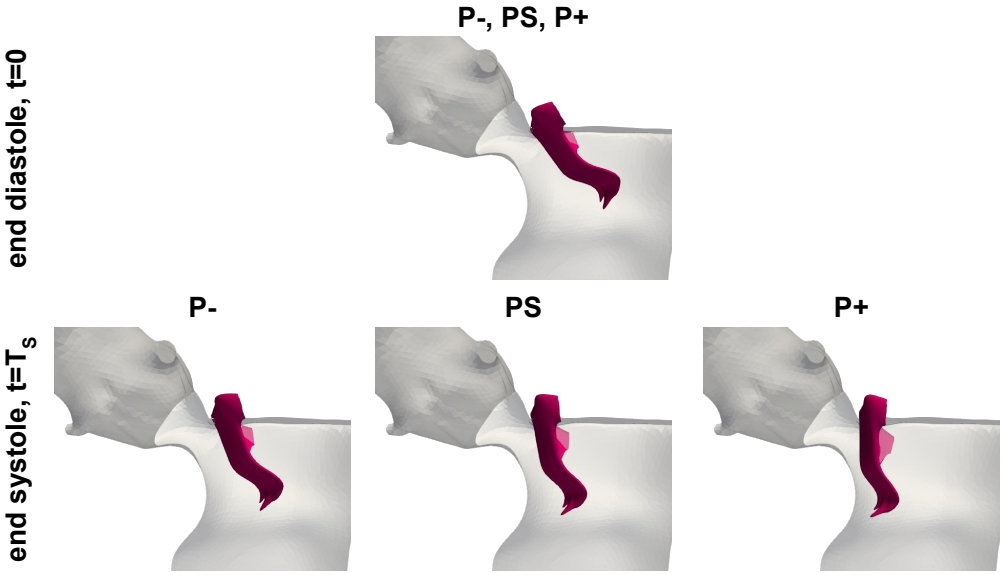

Figure 8: MV configurations at the end of diastole (above) and at the end of systole (below), for the three scenarios considered: P- (left), PS (center), P+ (right).

and two other virtual values representing a less severe ($\theta(T_S) = 15°$, P-) and a more severe ($\theta(T_S) = 35°$, P+) situation.

In Fig. 8, the reconstructed MV at end diastole and end systole are shown for the three scenarios P-, PS, P+. We observe that our method is able to provide significant MV configurations which could then be successfully used as geometric immersed data in our resistive CFD-ALE model.

In summary, our reconstructions allow us to obtain at each discrete time t^n the computational domain Ω^n and the moving ventricular wall $\Sigma^n_{v,w}$ together with its velocity $\mathbf{u}^n_{\text{MRI}}$ to be prescribed as Dirichlet condition, see (1). Regarding the moving aortic wall $\Sigma^n_{a,w}$ and the corresponding velocity, these are obtained by extrapolation of $\Sigma^n_{v,w}$ and $\mathbf{u}^n_{\text{MRI}}$. Completing the blood pool geometry, our reconstructions allowed us to identify the mitral valve orifice Σ^n_m. Notice that all these data are independent of the parametric end-diastolic angle $\theta(T_S)$ used in three scenarios P-, PS, P+. In addition, for each of such scenarios, we reconstruct the immersed MV leaflet Γ^n at each time t^n.

		P-	PS	P+
$\theta(T_S)$	[°]	15	25	35
$\max_{\mathbf{x}\in\Omega} \lvert\mathbf{u}(T_P,\mathbf{x})\rvert$	[m/s]	3.62	6.18	12.30
$\operatorname{avg}_{\mathbf{x}\in_{\text{inner}}^{\text{LV}}} p(T_P,\mathbf{x}) - p_o(T_P)$	[mmHg]	33	106	603

Table 3: Peak-systolic values of flow quantities for the three SAM-severity scenarios considered (P-, PS, P+). Pressure values are averaged over the LV-inner region (see Fig. 5-a).

4.2 Hemodynamics of systolic anterior motion

In this section we analyze the hemodynamics in the left ventricle and in the ascending aorta in the presence of SAM. In particular, we focus on the systolic phase and investigate the sensitivity of fluid dynamics quantities on the SAM severity parameter $\theta(T_S)$ introduced in Section 4.1 (cf. Fig. 8). The aim is to obtain possible indications about the development of the pathology and the appearance of secondary effects.

Starting from the geometries and motions reconstructed and reported in Section 4.1, the ALE displacement and velocity $\widehat{\mathbf{d}}_h^n, \widehat{\mathbf{u}}_{\text{ALE},h}^n$, $n = 0, 1, \ldots$, are introduced. We recall that during the systolic phase $t \in [0, T_S]$ the mitral orifice is closed. Moreover, a physiological pressure p_o is applied at the outflow section of the ascending aorta, with a peak value at time $T_P = 0.3$s (see Fig. 5-d).

In the following, the three scenarios P-, PS, P+ will be compared, in order to study how the level of severity of SAM affects the blood flow. Thanks to this comparison, we identify the effects of SAM alone, separating them from those due to the HOCM that concurs in the patient at hand.

In Fig. 9 the blood velocity field is represented on a 2D longitudinal slice to capture the SAM-induced hemodynamics near the mitral valve. We can observe that, in all the cases, the LVOT restriction due to the combination of septum hypertrophy and SAM yields a jet-like flow through the aortic orifice. Due to this jet structure, the characteristics of the flow in the rest of the ventricle can be considered having almost negligible influence on the flow patterns, apart from providing a flow rate that is consistent with systolic contraction.

Comparing the flows displayed in Fig. 9 for the different scenarios, one can notice that the intensity of the aforementioned jet grows with the level of SAM severity. This is shown also in Table 3, where increasing values of the peak-systolic maximum value of the velocity magnitude $\max_{\mathbf{x}\in\Omega} |\mathbf{u}(T_P,\mathbf{x})|$ are attained for increasing end-systolic leaflet angles $\theta(T_S)$. In this respect, we notice that the high values in the velocity observed for the P+ case are in accordance with the strong LVOT restriction that the displacement of the mitral leaflet determines.

About the pressure distribution in the ventricle and proximal aorta, Fig. 10 shows how SAM induces large pressure jumps in the LVOT: in comparison to

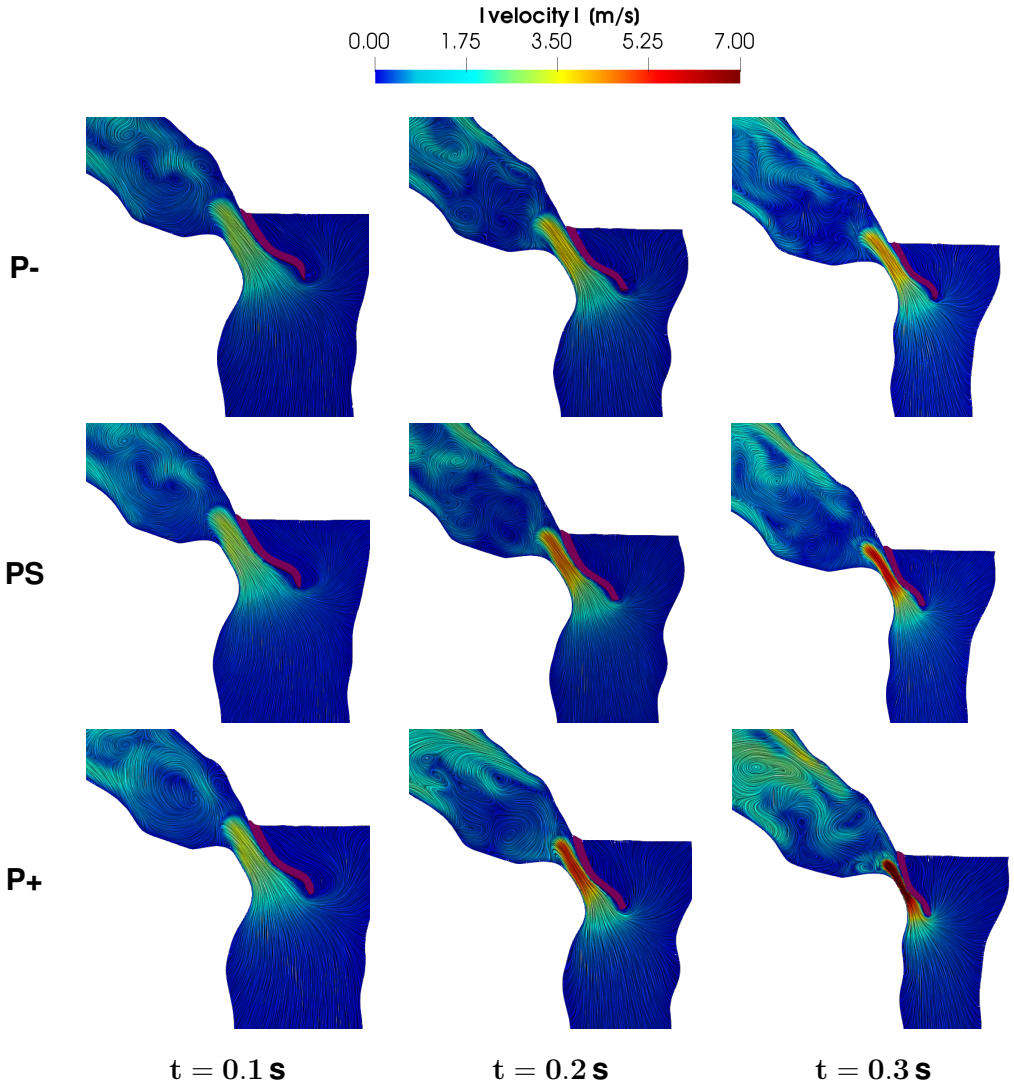

Figure 9: Representation of the velocity field on a 2D slice corresponding to the three-chambers MRI view at selected times ($t = 0.1\,\mathrm{s}, 0.2\,\mathrm{s}, 0.3\,\mathrm{s}$), for the three SAM-severity scenarios considered (P-, PS, P+).

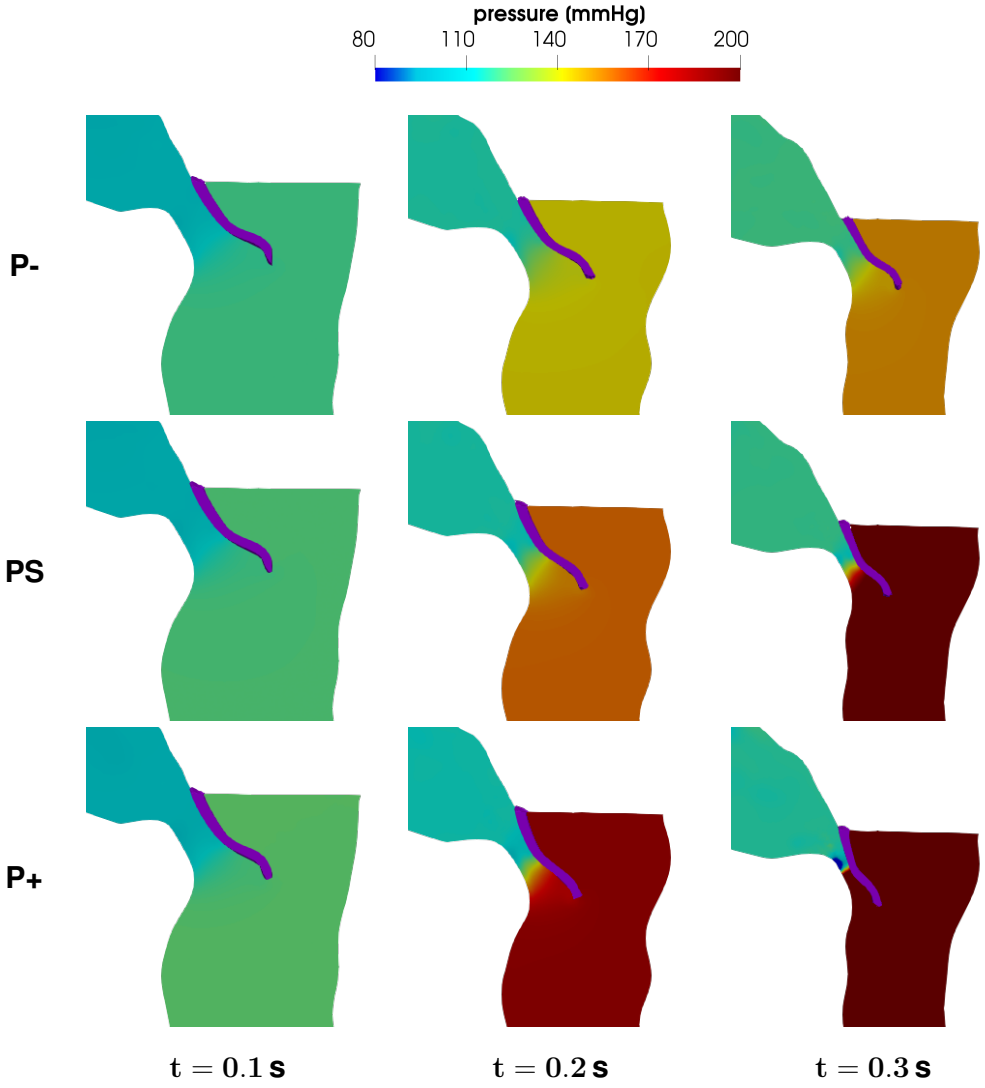

Figure 10: Representation of the pressure field on a 2D slice corresponding to the three-chambers MRI view at selected times ($t = 0.1\,\mathrm{s}, 0.2\,\mathrm{s}, 0.3\,\mathrm{s}$), for the three SAM-severity scenarios considered (P-, PS, P+).

$S(T_{\mathrm{P}})\,[10^5 \cdot \mathrm{s}^{-2}]$	P-	PS	P+
LVOT	5.62	13.6	44.2
aortic root	1.78	4.05	10.8
ascending aorta	1.19	1.74	2.84

Table 4: Peak-systolic values of the enstrophy density $S\,[10^5 \cdot s^{-2}]$ at $T_{\mathrm{P}} = 0.3\,s$. Values are computed over three different regions of the computational domain (LVOT, aortic root, and ascending aorta, see Fig. 5-a) for the three SAM-severity scenarios considered (P-, PS, P+).

these variations, the pressure distribution can be considered as uniform in the other regions of the computational domain. In particular, larger values of the pressure gradient are observed where the leaflet is nearer to the septum, thus yielding a stronger obstruction to the blood flow. Moreover, significant differences are noticeable among the pressure jumps of the three scenarios P-, PS, P+, both in the plots of Fig. 10 and in the peak-systolic values of Table 3, last row. This confirms the role of SAM in determining an intraventricular pressure jump, that is much higher than the subaortic stenosis due to the septum hypertrophy.

It is worth to point out that the pressure values obtained in the P+ case are much larger than in a physiological or even pathological condition. Indeed, this case represents an extreme situation. Including in our comparison the results obtained in such a condition allows the quantification of the effects of SAM on the flow, and thus to highlight the clinical importance of the assessment of this pathology.

In order to provide a more thorough description of the fluid dynamics with SAM, the vorticity of the flow and the Wall Shear Stress (WSS) are also inspected.

Concerning vorticity, Fig. 11 displays the vortical structures according to the Q-criterion (Hunt et al. 1988): contour lines of the quantity $Q = \frac{1}{2}\left(|W|_2 - |D|_2\right)$ are represented, where W and D are the skew-symmetric and the symmetric part of the velocity gradient, respectively. We can see that coherent structures develop in the aortic root, as a consequence of the jet flow entering from the aortic orifice, and that the intensity of these structures is strongly related to the SAM severity degree. In order to quantify such intensity, which is related to kinetic energy dissipation and possibly to transition to turbulence, we compute the average enstrophy density $S = \frac{1}{2|D|}\int_D |\nabla \times \mathbf{u}|^2$ in different regions $D \subset \Omega$. The values of S , at the systolic peak $T_{\mathrm{P}} = 0.3s$, are presented in Table 4. The high intensity of S in the LVOT is related to the strong jet flow, whose energy is then progressively dissipated while giving rise to the aforementioned structures in the aortic root, and then flowing through the ascending aorta. Comparing the values reported in the table for the different cases P-, PS, P+, we notice that vorticity is more pronounced if a more severe SAM condition is considered.

Regarding WSS, it is known that elevated values could be associated to a

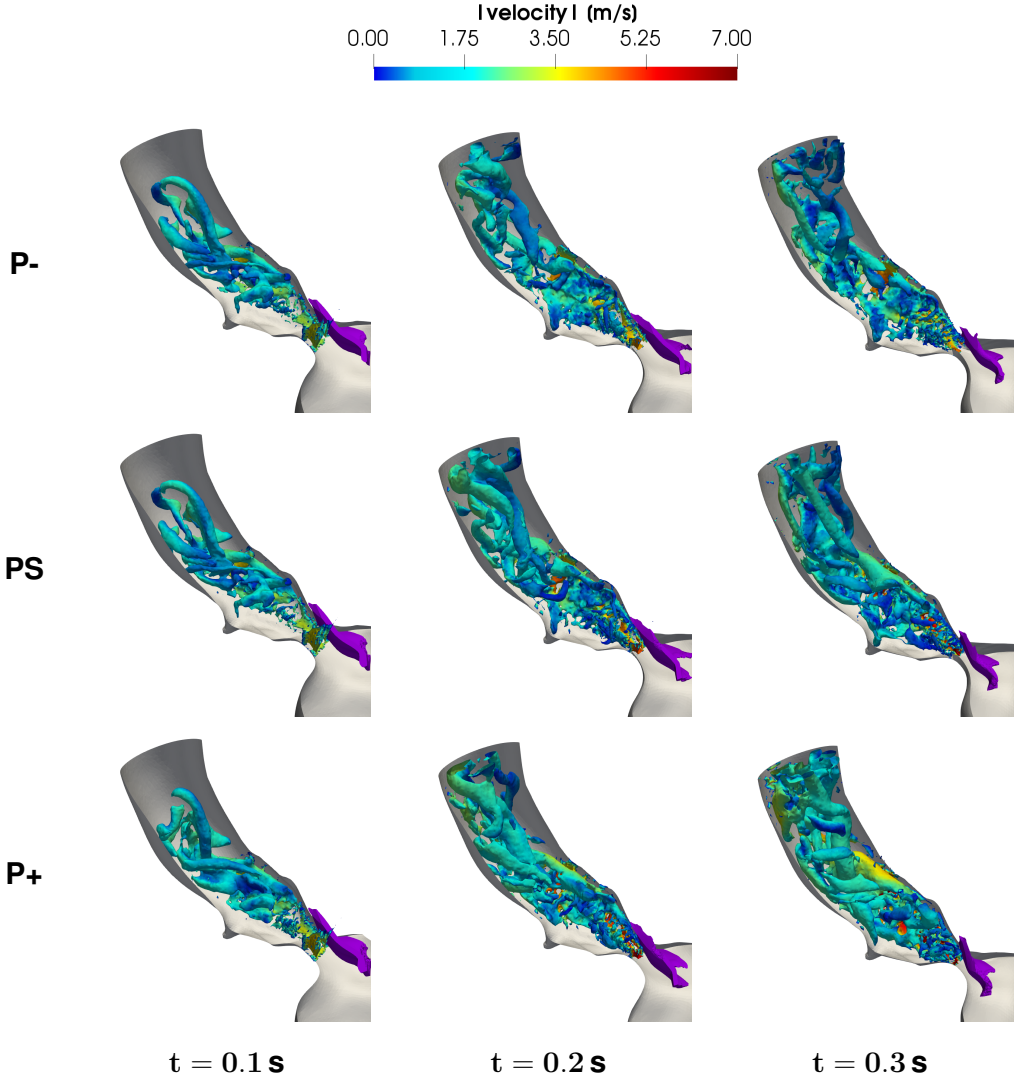

Figure 11: Representation of the Q-criterion contours ($Q = 0.013\,\mathrm{s}^{-1}$) colored by velocity magnitude at selected times ($t = 0.1\,\mathrm{s}, 0.2\,\mathrm{s}, 0.3\,\mathrm{s}$), for the three SAM-severity scenarios considered (P-, PS, P+).

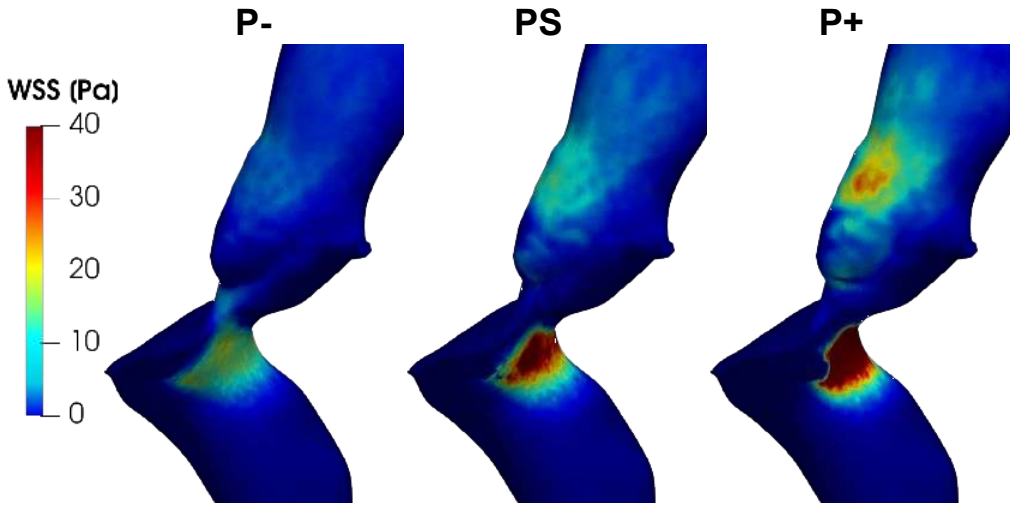

Figure 12: Wall Shear Stress (WSS) distribution at the systolic peak $t = 0.3$s, for the three SAM-severity scenarios considered (P-, PS, P+).

weakening of the vessel wall, thus creating conditions that may favour aneurysm formation (Dolan et al. 2013). Therefore, it is interesting to consider its distribution, displayed in Fig. 12 at the systolic peak $t = T_{\mathrm{P}}$. We notice that very high values are reached on the septal wall of the LVOT, as a consequence of the high-velocity flow in this region. As expected, the intensity of WSS increases with the severity of the SAM condition. Moreover, it is possible to identify also a region of the ascending aorta characterized by high WSS values. In this location, the jet flow coming from the LVOT impacts on the aortic wall and this impact is stronger in the case of a more severe SAM condition. This suggests that this region should be periodically monitored by clinical tests, in order to assess the risk of damage of the wall structure and thus prevent possible weakening and aneurysm formation.

4.3 Towards clinical indications

One of the most employed treatment for patients suffering from HOCM and SAM is septal myectomy, that is an open-heart intervention in which a portion of the interventricular septum is surgically removed. Under precise circumstances (Elliott et al. 2014), this procedure is typically characterized by low perioperative mortality and high long-term survival rate (Ommen et al. 2005; Maron and Nishimura 2014). Notice that, in critical conditions mitral valvuloplasty can be performed together with myectomy.

In this section, we want to provide preliminary quantitative indications that can help the surgeon in the preoperative design of the myectomy, in particular in determining the region and the size of the myocardium portion to be resected. In common practice, indeed, this decision is taken on the basis of diagnostic

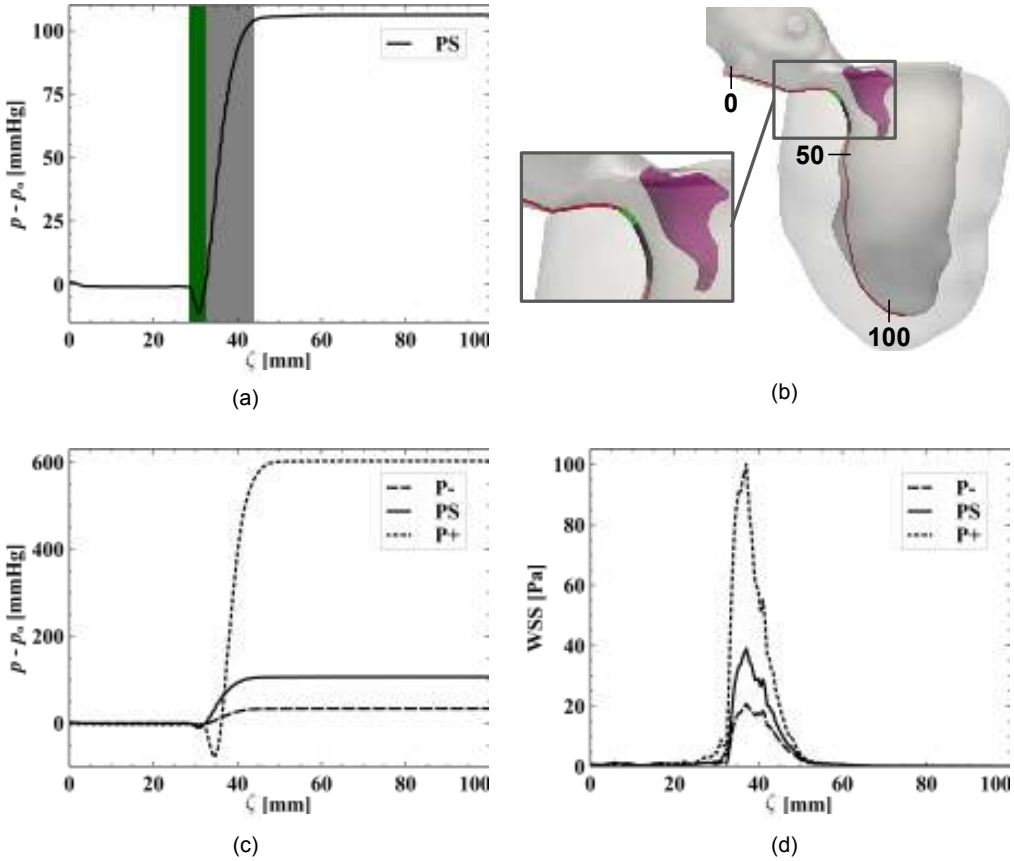

Figure 13: Profiles of pressure and wall shear stress on a line running along the septum with curvilinear coordinate ζ, from the aortic sinuses to the LV apex, at the systolic peak $T_{\mathrm{P}} = 0.3s$. (a) pressure profile for the PS case, with the regions discussed in Section 4.3 highlighted in green and grey; (b) position of the line along the septum parametrized by ζ, with a zoom on the LVOT; (c) pressure profiles for the cases P-, PS, P+; (d) wall shear stress profiles for the cases P-, PS, P+.

images and the surgeon's experience. Our results could provide more quantitative indications in this respect. More specifically, we focus on the pressure distribution on a line running along the septum wall, as displayed in Fig. 13-a,b. In this figure, the peak-systolic values of the difference $\Delta p = p - p_o$ of pressure w.r.t its aortic value is reported for the patient-specific case PS, against the curvilinear coordinate ζ that runs from the aorta to the apex along the septum. One can notice that the narrowing of the LVOT due to the hypertrophy of the septum yields a pressure drop in a region near to the aortic orifice (green region in Fig. 13-a). This is consistent with the Venturi effect that is often claimed to be the cause of SAM: the reduced pressure in the outflow tract of the ventricle drives the anterior mitral leaflet towards the septum. In the same figure, we can also observe that intraventricular pressure increases with ζ, with strong gradients in the subaortic region (especially in the grey region in Fig. 13-a) and reaching its maximum near the leaflet tip.

As a clinical indication, the present discussion identifies two regions of the LVOT (highlighted in Fig. 13-a,b) in which the surgical intervention may have positive outcomes: intervening in the green, low-pressure region (between $\zeta =$ 28mm and $\zeta = 32$mm in our case) can possibly dampen the Venturi effect causing SAM; on the other hand, removing a portion of the septum in the grey region (between $\zeta = 32$mm and $\zeta = 44$mm in our case) can reduce the large pressure gradients and the intraventricular stenosis. These sites are those commonly targeted in surgical practice for septal myectomy (Morrow et al. 1975; Elliott et al. 2014).

For completeness, in Fig. 13-c we also provide the pressure profiles for the other two cases P-, P+ considered in our parametric study. The differences among the three degrees of SAM severity are significantly large, therefore we can state that SAM has a major effect on the pressure levels inside the left ventricle. Moreover, this observation highlights the importance of an accurate reconstruction of the patient specific mitral valve configuration, in order to properly assess the severity of the condition.

We deem that also the analysis of the WSS could give indications about the location where to perform septal myectomy. For this reason, in Fig. 13-d we report its values on a line along the septum. In this representation, we can appreciate how the maximum value of WSS, attained at the narrowing, strongly depends on SAM severity, thus confirming the importance of a proper evaluation of this parameter in the assessment of SAM.

5 Conclusions

In the present work, a CFD study on the effects of SAM in presence of HOCM has been carried out. A novel reconstruction pipeline has been proposed to obtain the ventricle and mitral valve geometry and motion from kinetic imaging data. The blood flow in the reconstructed, moving domains has been modeled

with Navier-Stokes equations in ALE form, enhanced with a resistive method to represent the immersed mitral valve. The main outcomes of the present work can been summarized as follows:

- The proposed reconstruction pipeline has been effectively applied to standard cine-MRI data, which are routinely acquired in diagnostic procedures;
- Through a parametric study, the dependence of hemodynamic quantities on the level of SAM severity has been assessed. These results show that the subaortic stenosis due to the combination of HOCM and SAM yields a jet-like flow through the LVOT, with sensible pressure jumps and localized high WSS in the ascending aorta;
- Driven by a commonly employed surgical treatment of HOCM and SAM, namely septal myectomy, special attention has been paid to the distribution of pressure along the septum, in order to provide practical indications for the preoperative design phase.

The results of the present work give preliminary clinical indications that can supplement clinical data in the assessment of the condition and design of the treatment. Directions of further investigation may consider a wider set of patients, with different geometries and conditions, and then possibly devising a global score for SAM severity, that can help in classifying the patients and deciding whether and how to intervene on them.

Acknowledgements

The authors thank Prof. Antonio Corno, MD, for his valuable insight and suggestions on the clinical relevance of the present work.

References

Akiyama K, Naito Y, Kinoshita M, Ishii M, Nakajima Y, Itatani K, Miyazaki T, Yamagishi M, Yaku H, Sawa T (2017) Flow energy loss evaluation in a systolic anterior motion case after the Ross procedure. Journal of Cardiothoracic and Vascular Anesthesia 31(6):2118–2122

Alauzet F, Fabrèges B, Fernández MA, Landajuela M (2016) Nitsche-XFEM for the coupling of an incompressible fluid with immersed thin-walled structures. Computer Methods in Applied Mechanics and Engineering 301:300–335

Antiga L, Ene-Iordache B, Remuzzi A (2003) Computational geometry for patient-specific reconstruction and meshing of blood vessels from MR and CT angiography. IEEE Transactions on Medical Imaging 22(5):674–684

Antiga L, Piccinelli M, Botti L, Ene-Iordache B, Remuzzi A, Steinman DA (2008) An image-based modeling framework for patient-specific computational hemodynamics. Medical & Biological Engineering & Computing 46(11):1097

Astorino M, Gerbeau JF, Pantz O, Traore KF (2009) Fluid–structure interaction and multi-body contact: application to aortic valves. Computer Methods in Applied Mechanics and Engineering 198(45-46):3603–3612

Astorino M, Hamers J, Shadden SC, Gerbeau JF (2012) A robust and efficient valve model based on resistive immersed surfaces. International Journal for Numerical Methods in Biomedical Engineering 28(9):937–959

Basting S, Quaini A, Čanić S, Glowinski R (2017) Extended ALE method for fluid–structure interaction problems with large structural displacements. Journal of Computational Physics 331:312–336

Bavo A, Pouch AM, Degroote J, Vierendeels J, Gorman JH, Gorman RC, Segers P (2016) Patient-specific CFD simulation of intraventricular haemodynamics based on 3D ultrasound imaging. BioMedical Engineering OnLine 15:107

Bavo A, Pouch AM, Degroote J, Vierendeels J, Gorman JH, Gorman RC, Segers P (2017) Patient-specific CFD models for intraventricular flow analysis from 3D ultrasound imaging: Comparison of three clinical cases. Journal of Biomechanics 50:144–150

Bazilevs Y, Calo V, Cottrell J, Hughes T, Reali A, Scovazzi G (2007) Variational multiscale residual-based turbulence modeling for large eddy simulation of incompressible flows. Computer Methods in Applied Mechanics and Engineering 197(1-4):173–201

Bertagna L, Deparis S, Formaggia L, Forti D, Veneziani A (2017) The lifev library: engineering mathematics beyond the proof of concept. arXiv preprint arXiv:171006596

Besl PJ, McKay ND (1992) Method for registration of 3-d shapes. In: Sensor fusion IV: control paradigms and data structures, International Society for Optics and Photonics, vol 1611, pp 586–606

Boffi D, Gastaldi L (2003) A finite element approach for the immersed boundary method. Computers & Structures 81(8-11):491–501

Boilevin-Kayl L, Fernández MA, Gerbeau JF (2019a) A loosely coupled scheme for fictitious domain approximations of fluid-structure interaction problems with immersed thin-walled structures. SIAM Journal on Scientific Computing 41(2):B351–B374

Boilevin-Kayl L, Fernández MA, Gerbeau JF (2019b) Numerical methods for immersed FSI with thin-walled structures. Computers & Fluids 179:744–763

Borazjani I (2013) Fluid–structure interaction, immersed boundary-finite element method simulations of bio-prosthetic heart valves. Computer Methods in Applied Mechanics and Engineering 257:103–116

Borazjani I, Ge L, Sotiropoulos F (2010) High-resolution fluid–structure interaction simulations of flow through a bi-leaflet mechanical heart valve in an anatomic aorta. Annals of Biomedical Engineering 38(2):326–344

Cai L, Wang Y, Gao H, Ma X, Zhu G, Zhang R, Shen X, Luo X (2019) Some effects of different constitutive laws on simulating mitral valve dynamics with FSI. Scientific Reports 9:12753

Cheng R, Lai YG, Chandran KB (2004) Three-dimensional fluid-structure interaction simulation of bileaflet mechanical heart valve flow dynamics. Annals of Biomedical Engineering 32(11):1471–1483

Chnafa C, Mendez S, Nicoud F (2016) Image-based simulations show important flow fluctuations in a normal left ventricle: What could be the implications? Annals of Biomedical Engineering 44(11):3346–3358

Collia D, Vukicevic M, Meschini V, Zovatto L, Pedrizzetti G (2019) Simplified mitral valve modeling for prospective clinical application of left ventricular fluid dynamics. Journal of Computational Physics 398:108895

Crum WR, Hartkens T, Hill D (2004) Non-rigid image registration: theory and practice. The British Journal of Radiology 77(suppl_2):S140–S153

De Hart J, Peters G, Schreurs P, Baaijens F (2003) A three-dimensional computational analysis of fluid–structure interaction in the aortic valve. Journal of Biomechanics 36(1):103–112

Dedè L, Menghini F, Quarteroni A (2019) Computational fluid dynamics of blood flow in an idealized left human heart. International Journal for Numerical Methods in Biomedical Engineering p e3287

D'Elia M, Mirabella L, Passerini T, Perego M, Piccinelli M, Vergara C, Veneziani A (2011) Applications of variational data assimilation in computational hemodynamics. In: Ambrosi D, Quarteroni A, G R (eds) Modeling of Physiological Flows, Springer, pp 363–394

Deng L, Huang X, Yang C, Lyu B, Duan F, Tang D, Song Y (2018) Numerical simulation study on systolic anterior motion of the mitral valve in hypertrophic obstructive cardiomyopathy. International Journal of Cardiology 266:167–173

Dolan J, Kolega J, Meng H (2013) High wall shear stress and spatial gradients in vascular pathology: A review. Annals of Biomedical Engineering 41(7):1411–1427

Donea J, Giuliani S, Halleux JP (1982) An arbitrary Lagrangian-Eulerian finite element method for transient dynamic fluid-structure interactions. Computer Methods in Applied Mechanics and Engineering 33(1-3):689–723

Dos Santos ND, Gerbeau JF, Bourgat JF (2008) A partitioned fluid–structure algorithm for elastic thin valves with contact. Computer Methods in Applied Mechanics and Engineering 197(19-20):1750–1761

Elliott PM, Anastasakis A, Borger MA, Borggrefe M, Cecchi F, Charron P, Hagege AA, Lafont A, Limongelli G, Mahrholdt H, McKenna WJ, Mogensen J, Nihoyannopoulos P, Nistri S, Pieper PG, Pieske B, Rapezzi C, Rutten FH, Tillmanns C, Watkins H (2014) 2014 ESC guidelines on diagnosis and management of hypertrophic cardiomyopathy. European Heart Journal 35(39):2733–2779

Espino DM, Shepherd DE, Hukins DW (2014) Evaluation of a transient, simultaneous, arbitrary Lagrange–Euler based multi-physics method for simulating the mitral heart valve. Computer Methods in Biomechanics and Biomedical Engineering 17(4):450–458

Fedele M (2019) Polygonal surface processing and mesh generation tools for numerical simulations of the complete cardiac function. MOX report 32/2019

Fedele M, Faggiano E, Dedè L, Quarteroni A (2017) A patient-specific aortic valve model based on moving resistive immersed implicit surfaces. Biomechanics and Modeling in Mechanobiology 16(5):1779–1803

Feng L, Gao H, Griffith B, Niederer S, Luo X (2019) Analysis of a coupled fluid-structure interaction model of the left atrium and mitral valve. International Journal for Numerical Methods in Biomedical Engineering 35(11):e3254

Fernández MA, Gerbeau JF, Martin V (2008) Numerical simulation of blood flows through a porous interface. ESAIM: Mathematical Modelling and Numerical Analysis 42(6):961–990

Fetzer A, Zelzer S, Schroeder T, Meinzer HP, Nolden M (2014) An interactive 3D segmentation for the medical imaging interaction toolkit (MITK). Proc MICCAI Interactive Medical Image Computing p 11

Forti D, Dedè L (2015) Semi-implicit BDF time discretization of the Navier-Stokes equations with VMS-LES modeling in a high performance computing framework. Computers & Fluids 117:168–182

Gao H, Feng L, Qi N, Berry C, Griffith BE, Luo X (2017) A coupled mitral valve-left ventricle model with fluid-structure interaction. Medical Engineering & Physics 47:128–136

Ge L, Sotiropoulos F (2010) Direction and magnitude of blood flow shear stresses on the leaflets of aortic valves: is there a link with valve calcification? Journal of Biomechanical Engineering 132(1):014,505

Ge L, Leo HL, Sotiropoulos F, Yoganathan AP (2005) Flow in a mechanical bileaflet heart valve at laminar and near-peak systole flow rates: CFD simulations and experiments. Journal of Biomechanical Engineering 127(5):782–797

Griffith BE (2012) Immersed boundary model of aortic heart valve dynamics with physiological driving and loading conditions. International Journal for Numerical Methods in Biomedical Engineering 28(3):317–345

Griffith BE, Luo X, McQueen DM, Peskin CS (2009) Simulating the fluid dynamics of natural and prosthetic heart valves using the immersed boundary method. International Journal of Applied Mechanics 1(01):137–177

Hill DL, Batchelor PG, Holden M, Hawkes DJ (2001) Medical image registration. Physics in Medicine & Biology 46(3):R1

Hsu MC, Kamensky D, Bazilevs Y, Sacks MS, Hughes TJ (2014) Fluid–structure interaction analysis of bioprosthetic heart valves: significance of arterial wall deformation. Computational Mechanics 54(4):1055–1071

Hunt J, Wray A, Moin P (1988) Eddies, streams, and convergence zones in turbulent flows. Center for Turbulence Research Report CTR-S88:193–208

Iaccarino G, Verzicco R (2003) Immersed boundary technique for turbulent flow simulations. Applied Mechanics Reviews 56(3):331–347

Ibrahim M, Rao C, Ashrafian H, Chaudhry U, Darzi A, Athanasiou T (2012) Modern management of systolic anterior motion of the mitral valve. European Journal of Cardio-Thoracic Surgery 41(6):1260–1270

Jiang L, Levine RA, King ME, Weyman AE (1987) An integrated mechanism for systolic anterior motion of the mitral valve in hypertrophic cardiomyopathy based on echocardiographic observations. American Heart Journal 113(3):633–644

Kaiser AD, McQueen DM, Peskin CS (2019) Modeling the mitral valve. International Journal for Numerical Methods in Biomedical Engineering 35(11):e3240

Kamensky D, Hsu MC, Schillinger D, Evans JA, Aggarwal A, Bazilevs Y, Sacks MS, Hughes TJ (2015) An immersogeometric variational framework for fluid–structure interaction: Application to bioprosthetic heart valves. Computer Methods in Applied Mechanics and Engineering 284:1005–1053

Karamitsos TD, Francis JM, Myerson S, Selvanayagam JB, Neubauer S (2009) The role of cardiovascular magnetic resonance imaging in heart failure. Journal of the American College of Cardiology 54(15):1407–1424

Klein S, Staring M, Murphy K, Viergever MA, Pluim JP (2009) Elastix: a toolbox for intensity-based medical image registration. IEEE Transactions on Medical Imaging 29(1):196–205

Kunzelman K, Einstein DR, Cochran R (2007) Fluid–structure interaction models of the mitral valve: function in normal and pathological states. Philosophical Transactions of the Royal Society B: Biological Sciences 362(1484):1393–1406

Lassila T, Malossi C, Stevanella M, Votta E, Redaelli A, Deparis S (2017) Simulation of left ventricle fluid dynamics with mitral regurgitation from magnetic resonance images with fictitious elastic structure regularization. arXiv preprint arXiv:170703998

Le TB, Sotiropoulos F (2013) Fluid–structure interaction of an aortic heart valve prosthesis driven by an animated anatomic left ventricle. Journal of Computational Physics 244:41–62

Lee HY, Codella NC, Cham MD, Weinsaft JW, Wang Y (2009) Automatic left ventricle segmentation using iterative thresholding and an active contour model with adaptation on short-axis cardiac MRI. IEEE Transactions on Biomedical Engineering 57(4):905–913

van Loon R, Anderson PD, van de Vosse FN (2006) A fluid–structure interaction method with solid-rigid contact for heart valve dynamics. Journal of Computational Physics 217(2):806–823

Lu Y, Radau P, Connelly K, Dick A, Wright GA (2009) Segmentation of left ventricle in cardiac cine MRI: An automatic image-driven method. In: International Conference on Functional Imaging and Modeling of the Heart, Springer, pp 339–347

Ma X, Gao H, Griffith BE, Berry C, Luo X (2013) Image-based fluid–structure interaction model of the human mitral valve. Computers & Fluids 71:417–425

Marom G (2015) Numerical methods for fluid–structure interaction models of aortic valves. Archives of Computational Methods in Engineering 22(4):595–620

Maron BJ, Nishimura RA (2014) Surgical septal myectomy versus alcohol septal ablation. Circulation 130(18):1617–1624

Maron MS (2012) Clinical utility of cardiovascular magnetic resonance in hypertrophic cardiomyopathy. Journal of Cardiovascular Magnetic Resonance 14(1):13

Masci A, Alessandrini M, Forti D, Menghini F, Dedé L, Tomasi C, Quarteroni A, Corsi C (2020) A proof of concept for computational fluid dynamic analysis

of the left atrium in atrial fibrillation on a patient-specific basis. Journal of Biomechanical Engineering 142(1):011002

Massing A, Larson M, Logg A, Rognes M (2015) A Nitsche-based cut finite element method for a fluid-structure interaction problem. Communications in Applied Mathematics and Computational Science 10(2):97–120

Meyer M, Desbrun M, Schröder P, Barr AH (2003) Discrete differential-geometry operators for triangulated 2-manifolds. In: Visualization and mathematics III, Springer, pp 35–57

Mitchell JR, Wang J (2014) Expanding application of the Wiggers diagram to teach cardiovascular physiology. Advances in Physiology Education 38(2):170–175

Mittal R, Iaccarino G (2005) Immersed boundary methods. Annual Review of Fluid Mechanics 37:239–261

Mittal R, Seo J, Vedula V, Choi Y, Liu H, Huang H, Jain S, Younes L, Abraham T, George R (2016) Computational modeling of cardiac hemodynamics: Current status and future outlook. Journal of Computational Physics 305:1065–1082

Morrow AG, Reitz BA, Epstein SE, Henry WL, Conkle DM, Itscoitz SB, Redwood D (1975) Operative treatment in hypertrophic subaortic stenosis. techniques, and the results of pre and postoperative assessments in 83 patients. Circulation 52(1):88–102

Morsi YS, Yang WW, Wong CS, Das S (2007) Transient fluid–structure coupling for simulation of a trileaflet heart valve using weak coupling. Journal of Artificial Organs 10(2):96–103

Myerson SG (2012) Heart valve disease: investigation by cardiovascular magnetic resonance. Journal of Cardiovascular Magnetic Resonance 14(1):7

Myerson SG, d'Arcy J, Christiansen JP, Dobson LE, Mohiaddin R, Francis JM, Prendergast B, Greenwood JP, Karamitsos TD, Neubauer S (2016) Determination of clinical outcome in mitral regurgitation with cardiovascular magnetic resonance quantification. Circulation 133(23):2287–2296

Nicolò F, Lio A, Comisso M, Pantanella R, Scrofani R, Musumeci F (2019) Surgical treatment of hypertrophic obstructive cardiomyopathy. In: Cardiac Surgery Procedures, IntechOpen

Nobile F, Formaggia L (1999) A stability analysis for the arbitrary Lagrangian-Eulerian formulation with finite elements. East-West Journal of Numerical Mathematics 7:105–132

Nolden M, Zelzer S, Seitel A, Wald D, Müller M, Franz AM, Maleike D, Fangerau M, Baumhauer M, Maier-Hein L, Maier-Hein K, Meinzer H, Wolf I (2013) The medical imaging interaction toolkit: challenges and advances. International Journal of Computer Assisted Radiology and Surgery 8(4):607–620

Oliveira FP, Tavares JMR (2014) Medical image registration: a review. Computer Methods in Biomechanics and Biomedical Engineering 17(2):73–93

Ommen SR, Maron BJ, Olivotto I, Maron MS, Cecchi F, Betocchi S, Gersh BJ, Ackerman MJ, McCully RB, Dearani JA, Schaff HV, Danielson GK, Tajik AJ, Nishimura RA (2005) Long-term effects of surgical septal myectomy on survival in patients with obstructive hypertrophic cardiomyopathy. Journal of the American College of Cardiology 46(3):470–476

Otani T, Al-Issa A, Pourmorteza A, McVeigh ER, Wada S, Ashikaga H (2016) A computational framework for personalized blood flow analysis in the human left atrium. Annals of Biomedical Engineering 44(11):3284–3294

Peskin CS (1972) Flow patterns around heart valves: A numerical method. Journal of Computational Physics 10(2):252 – 271

Quarteroni A, Dede L, Manzoni A, Vergara C (2019) Mathematical Modelling of the Human Cardiovascular System-Data, Numerical Approximation, Clinical Applications. Cambridge University Press

Rickers C, Wilke NM, Jerosch-Herold M, Casey SA, Panse P, Panse N, Weil J, Zenovich AG, Maron BJ (2005) Utility of cardiac magnetic resonance imaging in the diagnosis of hypertrophic cardiomyopathy. Circulation 112(6):855–861

Seo JH, Vedula V, Abraham T, Lardo AC, Dawoud F, Luo H, Mittal R (2014) Effect of the mitral valve on diastolic flow patterns. Physics of Fluids 26(12):121,901

Sherrid MV, Balaram S, Kim B, Axel L, Swistel DG (2016) The mitral valve in obstructive hypertrophic cardiomyopathy: a test in context. Journal of the American College of Cardiology 67(15):1846–1858

Sotiropoulos F, Borazjani I (2009) A review of state-of-the-art numerical methods for simulating flow through mechanical heart valves. Medical & biological engineering & computing 47(3):245–256

Su B, Zhong L, Wang XK, Zhang JM, San Tan R, Allen JC, Tan SK, Kim S, Leo HL (2014) Numerical simulation of patient-specific left ventricular model with both mitral and aortic valves by FSI approach. Computer Methods and Programs in Biomedicine 113(2):474–482

Suri JS (2000) Computer vision, pattern recognition and image processing in left ventricle segmentation: The last 50 years. Pattern Analysis & Applications 3(3):209–242

Tagliabue A, Dedè L, Quarteroni A (2017) Complex blood flow patterns in an idealized left ventricle: a numerical study. Chaos: An Interdisciplinary Journal of Nonlinear Science 27(9):093,939

Taira K, Colonius T (2007) The immersed boundary method: a projection approach. Journal of Computational Physics 225(2):2118–2137

Tan LK, Liew YM, Lim E, McLaughlin RA (2017) Convolutional neural network regression for short-axis left ventricle segmentation in cardiac cine MR sequences. Medical Image Analysis 39:78–86

Tezduyar T, Sathe S (2003) Stabilization parameters in SUPG and PSPG formulations. Journal of Computational and Applied Mechanics 4(1):71–88

This A (2019) Image/model fusion for the quantification of mitral regurgitation severity. PhD thesis, Université Pierre et Marie Curie

This A, Morales HG, Bonnefous O, Fernández MA, Gerbeau JF (2020) A pipeline for image based intracardiac CFD modeling and application to the evaluation of the PISA method. Computer Methods in Applied Mechanics and Engineering 358:112,627

To AC, Dhillon A, Desai MY (2011) Cardiac magnetic resonance in hypertrophic cardiomyopathy. JACC: Cardiovascular Imaging 4(10):1123–1137

Tran PV (2016) A fully convolutional neural network for cardiac segmentation in short-axis MRI. arXiv preprint arXiv:160400494

Votta E, Le TB, Stevanella M, Fusini L, Caiani EG, Redaelli A, Sotiropoulos F (2013) Toward patient-specific simulations of cardiac valves: state-of-the-art and future directions. Journal of Biomechanics 46(2):217–228

Wiggers CJ (1923) Modern aspects of the circulation in health and disease. Lea & Febiger

Wolf I, Vetter M, Wegner I, Böttger T, Nolden M, Schöbinger M, Hastenteufel M, Kunert T, Meinzer HP (2005) The medical imaging interaction toolkit. Medical Image Analysis 9(6):594–604

Wu MC, Zakerzadeh R, Kamensky D, Kiendl J, Sacks MS, Hsu MC (2018) An anisotropic constitutive model for immersogeometric fluid–structure interaction analysis of bioprosthetic heart valves. Journal of Biomechanics 74:23–31

Yoganathan AP, Chandran K, Sotiropoulos F (2005) Flow in prosthetic heart valves: state-of-the-art and future directions. Annals of Biomedical Engineering 33(12):1689–1694

Yu Z (2005) A DLM/FD method for fluid/flexible-body interactions. Journal of Computational Physics 207(1):1–27

Zonca S, Vergara C, Formaggia L (2018) An unfitted formulation for the interaction of an incompressible fluid with a thick structure via an XFEM/DG approach. SIAM Journal on Scientific Computing 40(1):B59–B84

Zygote Media Group, Inc (2014) Zygote solid 3D heart generation II development report. Tech. rep.

MOX Technical Reports, last issues

Dipartimento di Matematica
Politecnico di Milano, Via Bonardi 9 - 20133 Milano (Italy)

13/2020 Pozzi S.; Domanin M.; Forzenigo L.; Votta E.; Zunino P.; Redaelli A.; Vergara C.
A data-driven surrogate model for fluid-structure interaction in carotid arteries with plaque

14/2020 Calissano, A.; Feragen, A; Vantini, S.
Populations of Unlabeled Networks: Graph Space Geometry and Geodesic Principal Components

12/2020 Azzolin, L.; Dede', L.; Gerbi, A.; Quarteroni, A.
Effect of fibre orientation and bulk value on the electromechanical modelling of the human ventricles

11/2020 Antonietti, P.F.; Facciola', C.; Houston, P.; Mazzieri, I.; Pennes, G.; Verani, M.
High-order discontinuous Galerkin methods on polyhedral grids for geophysical applications: seismic wave propagation and fractured reservoir simulations

10/2020 Bonaventura, L.; Carlini, E.; Calzola, E.; Ferretti, R.
Second order fully semi-Lagrangian discretizations of advection--diffusion--reaction systems

09/2020 Rea, F.; Ieva, F.,; Pastorino, U.; Apolone, G.; Barni, S.; Merlino, L.; Franchi, M.; Corrao, G.
Number of lung resections performed and long-term mortality rates of patients after lung cancer surgery: evidence from an Italian investigation

08/2020 Antonietti, P. F.; Facciolà, C.; Verani, M.
Polytopic Discontinuous Galerkin methods for the numerical modelling of flow in porous media with networks of intersecting fractures

05/2020 Artioli, E.; Beiraoda Veiga, L.; Verani, M.
An adaptive curved virtual element method for the statistical homogenization of random fibre-reinforced composites

07/2020 Fumagalli, A.; Scotti, A.
Reactive flow in fractured porous media

06/2020 Domanin, M.; Piazzoli, G.; Trimarchi, S.; Vergara, C.
Image-based displacements analysis and computational blood dynamics after endovascular aneurysm repair